EFFECTIVE MODELING APPROACHES FOR CO_2 EOR DEVELOPMENTS

A Thesis

by

TSUBASA ONISHI

Submitted to the Office of Graduate and Professional Studies of
Texas A&M University
in partial fulfillment of the requirements for the degree of

MASTER OF SCIENCE

Chair of Committee,	Akhil Datta-Gupta
Committee Members,	Michael J. King
	Binayak, Mohanty
Head of Department,	A. Daniel Hill

December 2017

Major Subject: Petroleum Engineering

ABSTRACT

We present a simulation study of a mature reservoir for CO_2 Enhanced Oil Recovery (EOR) development. This project is currently recognized as the world's largest project utilizing post-combustion CO_2 from power generation flue gases. With a fluvial formation geology and sharp hydraulic conductivity contrasts, this is a challenging and novel application of CO_2 EOR. The objective of this study is to obtain a reliable predictive reservoir model by integrating multi-decadal production data at different temporal resolutions into the available geologic model. This will be useful for understanding flow units, heterogeneity features and their impact on subsurface flow mechanisms to guide the optimization of the injection scheme and maximize CO_2 sweep and oil recovery from the reservoir.

Our strategy consists of a hierarchical approach for geologic model calibration incorporating available pressure and multiphase production data. The model calibration is carried out using regional multipliers whereby the regions are defined using a novel Adjacency Based Transform (ABT) accounting for the underlying geologic heterogeneity. The Genetic Algorithm (GA) is used to match 70-year pressure and cumulative production by adjusting pore volume and aquifer strength. This leads to an efficient and robust workflow for field scale history matching.

The history matched model provided important information about reservoir volumes, flow zones and aquifer support that led to additional insight to the prior geological and simulation studies. The history matched field-scale model is used to define and initialize a detailed fine-scale model for a CO_2 pilot area which will be utilized for

studying the impact of fine-scale heterogeneity on CO_2 sweep and oil recovery. The uniqueness of this work is the application of a novel geologic model parameterization and history matching workflow for modeling of a mature oil field with decades of production history and which is currently being developed with CO_2 EOR.

In addition to the history matching studies, we developed an embedded discrete fracture model (EDFM) which is currently recognized as a promising alternative to conventional fracture modeling approaches including multiple continuum models and unstructured discrete fracture models because of its accuracy and computational efficiency. We tested the developed model with several examples including water flood and CO_2 flood scenarios and confirmed applicability of the EDFM.

DEDICATION

To my parents

ACKNOWLEDGEMENTS

I would like to express my utmost gratitude to my advisor, Dr. Datta-Gupta for his invaluable suggestions towards the completion of this research. I am likewise thankful to Dr. King for his advice. It was also a great privilege to have Dr. Mohanty as a member of my committee. I owe great gratitude to Feyi Olalotiti-Lawal, Nozomu Yoshida, and Atsushi Iino, my wonderful mentors. Also, my appreciation goes to the MCERI research consortium members.

CONTRIBUTORS AND FUNDING SOURCES

Contributors

This work was supported by a thesis committee consisting of Dr. Datta-Gupta and Dr. King of the Department of Petroleum Engineering and Dr. Mohanty of the Biological and Agricultural Engineering.

The work related to the Petra Nova project, presented in Chapter I-III is a collaborative project with JX Nippon.

All other work conducted for the thesis was completed by the student independently.

Funding Sources

Graduate study was supported by the MCERI research consortium members.

TABLE OF CONTENTS

Page

LIST OF FIGURES

Page

LIST OF TABLES

Page

CHAPTER I

INTRODUCTION*

1.1 Introduction to the Problem

Worldwide only a few large scale CCUS projects involving the capture and injection of anthropogenic CO_2 for the purpose of moving residual oil have been successfully operated. A prominent one being the Weyburn project which began in late 2000 in Saskatchewan Canada. The injected CO_2, sourced from a gasification plant in North Dakota USA, has helped increase oil production from the field by 60% within a decade of operation (Whittaker, et al. 2011). A gross amount of over 30 million tons of CO_2 is projected to be geologically stored in 2030 when the project is expected to end. The success of the Weyburn project in terms of both economic and environment benefits has inspired the start of many other large scale industrially sourced CO_2 EOR projects across the globe. The number of operational projects in the last 17 years has tripled compared to what existed prior to Weyburn (GCCS 2015). Many more projects are at different stages of planning and construction and most are expected to commence operations by the end of the decade.

* Part of this section is reprinted with permission from "Post-Combustion CO_2 EOR Development in a Mature Oil Field: Model Calibration Using a Hierarchical Approach" by Feyi Olalotiti Lawal, Tsubasa Onishi, Akhil Datta-Gupta, Yusuke Fujita, and Kenji Hagiwara. 2017. SPE Annual Technical Conference and Exhibition, 9-11 October, San Antonio, Texas. Copyright 2017 Society of Petroleum Engineers

A crucial aspect of these projects is not only identifying mature oil fields suitable for CO_2 EOR, but also understanding the subsurface environment for better management of the project. Reservoir pressure is known to have a great impact on the CO_2 phase behavior which in turn influences the overall reservoir performance. Equally important is the multiphase flow physics of the system which needs to be properly understood to improve sweep efficiency during CO_2 injection. More so, for high permeability contrast systems where complexities involved with three phase flow systems are quickly magnified (Madiebo, Nasrabadi and Gildin 2015). For this purpose, it is customary to develop subsurface models that provide reliable description of the reservoir performance. Such models are typically a product of the integration of multiple sources of data, for example, production and downhole pressure responses and time-lapse seismic measurements.

1.2 History Matching Techniques

A systematic approach to reservoir model calibration has been shown to follow a hierarchical (Yin, et al. 2011) approach which requires a global reservoir energy calibration in the first step followed by local changes in model pertrophysical properties. Reservoir model features such as local pore volumes, transmissibility multipliers and aquifer strength are calibrated in this step to match the reservoir pressure. The local calibration step tunes grid properties such as permeability to match local fractional flow profiles at producer wells (He, Yoon and Datta-Gupta 2002, Bhark, Rey, et al. 2011). Bhark, Rey, et al. (2011) successfully applied this methodology to a turbidite reservoir in the Gulf of Mexico. History matching problems have also been approached from multi-objective (Park, Datta-Gupta and King 2014) and probabilistic (Ma, et al. 2008, Olalotiti-Lawal and Datta-Gupta 2015) standpoint for

improved analysis of calibrated reservoir models. The quality and robustness of all model calibration workflows hinges on proper and effective model parametrization, guided by prior parameter sensitivity studies. Reservoir models are increasingly becoming larger with cell counts already in the order of millions. Adjusting parameters in all these cells independently to match observed reservoir response is not only computational intractable, it is also likely to result in overfitted models with potential loss of geologic realism.

1.3 Model Parameterization

Model reparameterization techniques have been developed to address this difficulty through a spectral representation of the reservoir cell properties. A widely applied parameterization technique is the Karhunen-Loeve Transform (KLT) (Leverett 1941) which updates reservoir grid properties using a set of eigenvectors obtained from an eigen-decompostion of the parameter covariance matrix. (Jafarpour and McLauglin 2009) later proposed the application of Discrete Cosine Transforms (DCT) (Strang 1999) to circumvent the need for a prior covariance matrix which may not be reliable. In this method, the covariance matrix is replaced by a grid connectivity Laplacian. This concept was generalized by Bhark, Jafarpour, et al. (2011) to fully account for complex gridding such as corner point and unstructured grid as well as faulted geometry used to represent realistic structural features in reservoir models.

1.4 Research Objectives

This work presents a field application of effective reparameterization techniques for robust model calibration. We apply our model calibration workflow to the Petra Nova project

involving large scale industrially sourced CO_2 EOR. Petra Nova, a 50/50 joint venture between NRG and JX Nippon operates a commercial-scale post-combustion carbon capture facility at NRG's WA Parish generating station southwest of Houston, Texas. This facility captures more than 90 percent of the CO_2 from a 240 MW slipstream of flue gas. This is the world's largest post-combustion carbon capture facility installed on an existing coal-fueled power plant. The captured CO_2 is being utilized for Enhanced Oil Recovery to increase production at the West Ranch oil field, which is operated by Hilcorp Energy Company. The field was discovered in 1938 and has been in continuous operation ever since. Since then, it has produced approximately 390 million barrels of oil. Facility construction was commenced after the investment decision in 2014. Pre-EOR water injection was initiated in mid 2016 for pressurizing the target reservoir and then CO_2 injection was commenced at the end of 2016.

The objective of this study was to calibrate the reservoir model and match the reservoir pressure/energy over the period of prolonged depletion of the reservoir, and then update the model permeability field by utilizing the more recent water injection and pressure data used for repressurization. Spectral reparameterization methods were applied in both steps of the model calibration process. In the first step, we applied the Adjacency Based Transform (Bhark, Datta-Gupta and Jarapour 2011) in defining reservoir pore volume multiplier regions based on the underlying geological and structural features of the model. Reservoir energy was calibrated in the first step involving over 70 years of production from over 130 wells. The model permeability was updated utilizing the GCT reprarametrization approach. Only modest changes to prior permeability field ware required to match the fluid injection data. This paper is organized as follows: first we provide a quick description of the problem we address, and the procedure involved. This includes a methodical upscaling of the geologic model and its

validation using streamline-based techniques. A detailed sensitivity studies on parameters potentially impacting subsurface flow dynamics follows, and next the model energy calibration step. This is referred to as the first stage of our hierarchical model calibration workflow. Finally, we present the second stage involving the model permeability update and the validation of the final calibrated model.

CHAPTER II

MODEL DESCRIPTION*

2.1 Geologic Model

We carried out all simulations runs using the Exploration Consultants Limited Implicit Program for Simulation Engineering in a native format (ECLIPSE) (Schlumberger 2014). The geologic model has 252 × 212 × 140 grid discretization (3 million cells are active) with average cell dimensions of 152.4 × 152.4 × 3.0 m. The fluvial reservoir under study has large permeability contrasts at varying length scales, ranging from 0.5 to 35,000mD. With a Dykstra-Parsons heterogeneity measure of over 0.9, the reservoir can be categorized as highly heterogeneous (Willhite 1986). The intermittent stratigraphic shale barriers and baffles contribute to severe vertical permeability anisotropy in the formation. Grid petrophysical properties and fluid contacts in the geologic model are shown Error! Reference source not ound.. The model did not include a small portion of the reservoir sands in the upper part of the formation that would contain most of the gas cap due to dearth of data.

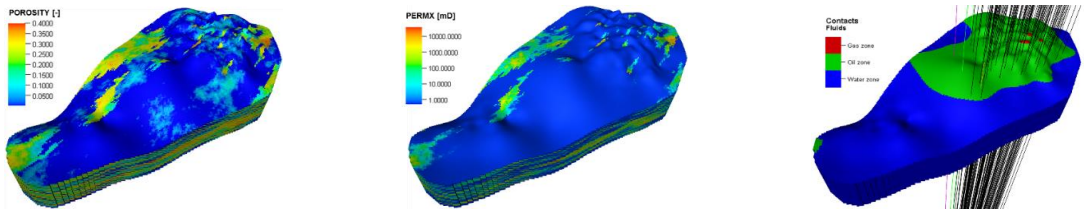

(a) (b) (c)

Figure 2.1: Geologic model showing (a) porosity field, (b) permeability field and (c) fluid contact at virgin reservoir conditions. More than 130 wells have drained the reservoir over a 70-year period

* Part of this section is reprinted with permission from "Post-Combustion CO_2 EOR Development in a Mature Oil Field: Model Calibration Using a Hierarchical Approach" by Feyi Olalotiti Lawal, Tsubasa Onishi, Akhil Datta-Gupta, Yusuke Fujita, and Kenji Hagiwara. 2017. SPE Annual Technical Conference and Exhibition, 9-11 October, San Antonio, Texas. Copyright 2017 Society of Petroleum Engineers

2.2 Fluid Model

The fluids modeled for our study are described by aqueous, organic, and gaseous phases with a black oil model obtained from the PVTSIM (Calsep) and assumed to be an isothermal system. Properties of oils and gases as a function of pressure are provided in **Figure 2.2.**

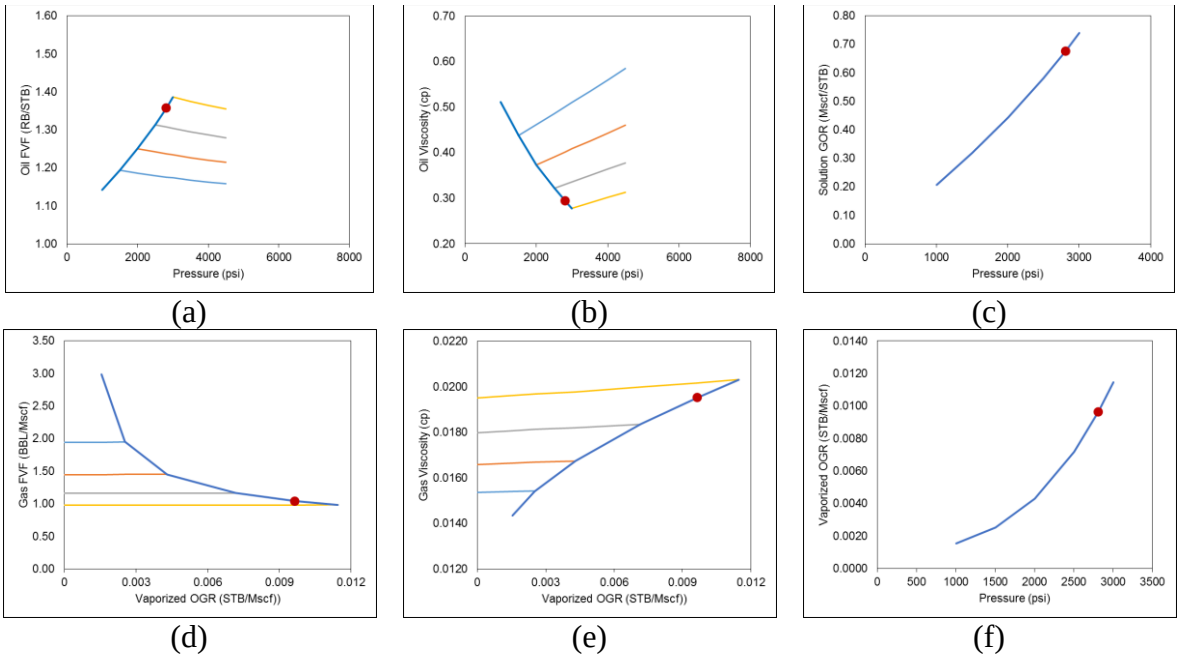

Figure 2.2: PVT table showing (a) oil formation volume factor, (b) oil viscosity, (c) solution gas oil ratio, (d) gas formation volume factor, (e) gas viscosity, (f) vaporized GOR

In our approach, the Brook-Corey equations (Brooks and Corey 1964) are applied for relative permeability curves.

$$k_{rw} = k_{rw}^{0}\left(\frac{S_w - S_{wc}}{1.0 - S_{or} - S_{wc} - S_{gc}}\right)^{n_w} \tag{2.1}$$

$$k_{ro} = k_{ro}^{0}\left(\frac{S_o - S_{or}}{1.0 - S_{or} - S_{wc} - S_{gc}}\right)^{n_o} \tag{2.2}$$

$$k_{rg} = k_{rg}^{0}\left(\frac{S_g - S_{gc}}{1.0 - S_{or} - S_{wc} - S_{gc}}\right)^{n_g} \tag{2.3}$$

where, $k_{r,l}^{0}$ is the end-point relative permeability of phase *l*, S_l is the saturation of phase *l*, S_{lr} is the residual saturation of phase *l*, S_{lc} is the connate saturation of phase *l*, and n_l is the curvature exponents of phase *l*. **Table 2.1** presents values of the base case for Eqs. 2.1 to 2.3 based on previously performed core analysis and **Figure 2.3** shows computed three phase relative permeability curves.

Table 2.1. Parameters in the relative permeability model for the base case

Parameter	Values
Oil-water	
End-point water relative permeability, k_{rw}^{0} (-)	0.90
End-point oil relative permeability, k_{ro}^{0} (-)	1.00
Exponent for water relative permeability, n_w (-)	3.00
Exponent for oil relative permeability, n_o (-)	2.00
Connate water saturation, S_{wc} (-)	0.28
Residual oil saturation, S_{or} (-)	0.15
Gas-Liquid	
End-point gas relative permeability, k_{rg}^{0} (-)	0.80
End-point oil relative permeability, k_{ro}^{0} (-)	1.00
Exponent for gas relative permeability, n_g (-)	2.00
Exponent for oil relative permeability, n_o (-)	4.00
Connate gas saturation, S_{wc} (-)	0.00
Connate liquid saturation, S_{lc} (-)	0.43

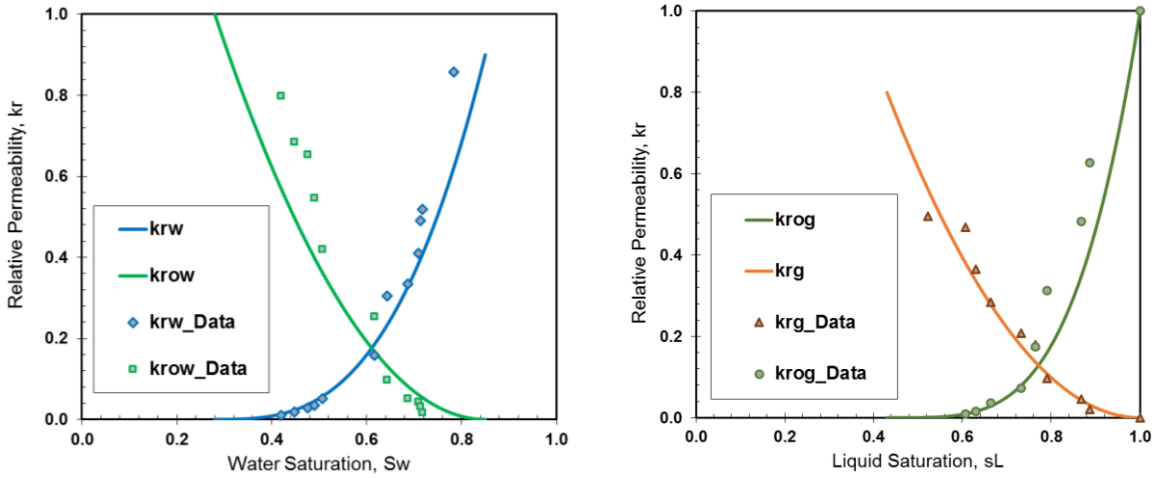

(a) (b)

Figure 2.3: Relative permeability curves (a) oil-water and (b) gas-liquid

2.3 Production History

Production began from the field in early 1940 under primary depletion which lasted until early 1970s. The reservoir was thereafter placed on a waterflood scheme for another 10 years until field water cut rose above economic levels. The field has since been operated under primary depletion. A graphic summary of the production and injection profile, including surface multiphase production, water injection, and average reservoir pressure is provided in **Figure 2.4**. The steady rise in average reservoir pressure provides an apparent indication of an external source of energy support, possibly from an aquifer. The production profile clearly exhibits a classical behavior with low initial water production to close to 100% water cut eventually.

More than 130 wells have been drilled and completed in the formation over the life of the reservoir. However, very limited information exists on the individual well production and completion data. Our flow simulation approach therefore constrains the reservoir to the

available total production sand injection volumes and allocates fluxes to wells and completion according to their respective productivity indices. Although not shown here, additional reservoir pressurization data over a period of 1year was also provided. During this period, water and CO_2 are injected into the formation to raise the average pressure above the minimum miscibility pressure in preparation for the CO_2 EOR scheme. Downhole pressure data were taken at high temporal resolutions in two monitor wells. The objective of the reservoir model calibration is to match the pressure/energy of the reservoir by integrating the 70year+ production data and then update the model permeability field by integrating the recently acquired reservoir pressurization data.

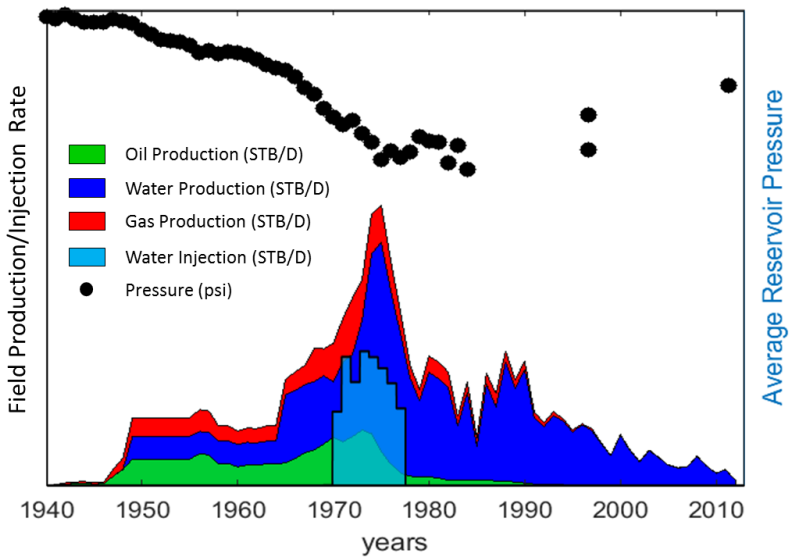

Figure 2.4: Fluid production and average pressure of the reservoir from 1940 to 2012

CHAPTER III

RESERVOIR ENERGY CALIBRATION*

3.1 Introduction

The geologic model with high heterogeneity and large number of gridblocks (~7.5 million) is computationally demanding. Specifically, it can take more than a month to run a single simulation over 70 years of duration. It was therefore necessary to upscale the geologic model to improve the simulation efficiency prior to carrying out the reservoir pressure and energy calibration. This chapter presents upscaling methodologies we applied, followed by the reservoir energy calibration using a novel geologic model parameterization techniques.

3.2 Geologic Model Upscaling

Through the use of sophisticated geological and geostatistical modeling tools based on core data, well logs, and seismic data, geologists and engineers can generate a high-resolution geologic model which are important for reservoir management. Although accurate, the direct use of these high resolution models for reservoir simulation is not computationally feasible because subsequent steps such as history matching and optimizations can require hundreds of reservoir simulations (Durlofsky, et al. 1996, Li and Becker 2000). Upgridding and upscaling methodologies are therefore developed to enhance computational efficiency.

* Part of this section is reprinted with permission from "Post-Combustion CO_2 EOR Development in a Mature Oil Field: Model Calibration Using a Hierarchical Approach" by Feyi Olalotiti Lawal, Tsubasa Onishi, Akhil Datta-Gupta, Yusuke Fujita, and Kenji Hagiwara. 2017. SPE Annual Technical Conference and Exhibition, 9-11 October, San Antonio, Texas. Copyright 2017 Society of Petroleum Engineers

If coarsened too far, the reservoir may lose geologic realism while cost of the simulation model may remain too high if coarsened little. Therefore, it is desired to find an optimal coarsening scheme (King, et al. 2005).

For our application, a combination of layer and areal coarsening was required to reduce the computational cost required for the history matching step. The areal coarsening approach follows a regular structured upgridding (for instance 3x3, 5x5 areal upgridding), while for the layer upgridding we adopted the optimal layer coarsening approach heterogeneity (King, et al. 2005, X. Ma 2008, S. Du 2012). The recursive sequential coarsening scheme only merges neighboring layers that result in the least reduction in a predefined measure of total variation of heterogeneity as given below:

$$H = \sum_{i,j,k=1}^{NX,NY,NZ} n_{i,j,k}\left(P_{i,j,k} - \bar{P}_{i,j}\right)^2 \quad (3.1)$$

And,

$$\bar{P}_{i,j} = \sum_{k=1}^{NZ} n_{i,j,k} \bullet P_{i,j,k} \Big/ \sum_{k=1}^{NZ} n_{i,j,k} \quad (3.2)$$

where $n_{i,j,k}$ denotes the net rock volume of the cell. Use of $n_{i,j,k}$ is to ensure that the measure of heterogeneity does not change under numerical refinement of the grid. The property $P_{i,j,k}$ represents a proxy for flow speed given by cell permeability to porosity ratio which is a combination of the local speed (k/ϕ) and the local slowness (ϕ/k). $\bar{P}_{i,j}$ is simply a bulk volume weighted average of $P_{i,j,k}$ for the (i, j) grid pillar. The optimal layer coarsening algorithm consists of two major steps. First, we compute loss of heterogeneity between

adjacent layer pairs, (δW). A pair with minimum δW will be merged into a single layer and repeat this procedure until the model becomes a single layer. Second step is to find an optimal number of layer which is defined as the minimum number of layers that can preserve major. This approach allows users to specify the maximum number of layers to be merged into a single layer. In our approach, we used three values including 6, 8, and 12 resulting in 31, 23, and 17 layers, respectively. **Figure 3.1** presents variation of heterogeneity and cross-sections of upscaled permeability and porosity fields at different vertical are provided for visual comparison in **Figure 3.2**, **Figure 3.4** and **Figure 3.3**. Structured grid coarsening in areal direction was also carried out aerially to further reduce number of cells. The final upgridding scheme then forms the framework on which transmissibility upscaling was carried out for all flow simulation purposes.

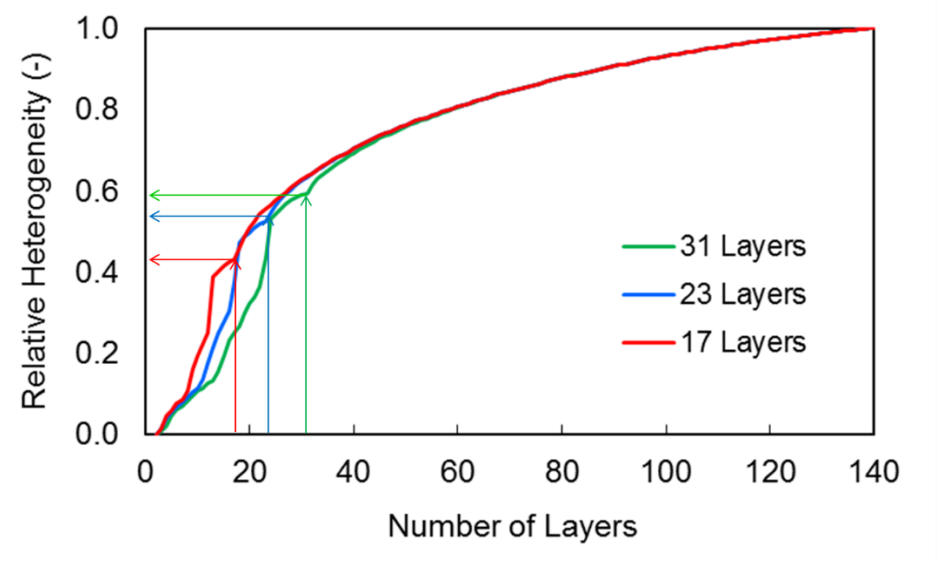

Figure 3.1: Varation of heterogeneity

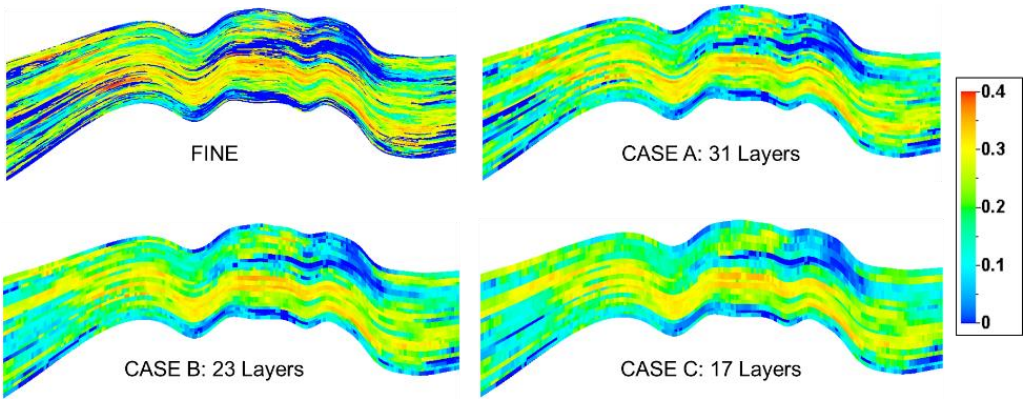

Figure 3.2: Comparsion of fine scale and upscaled porosity field

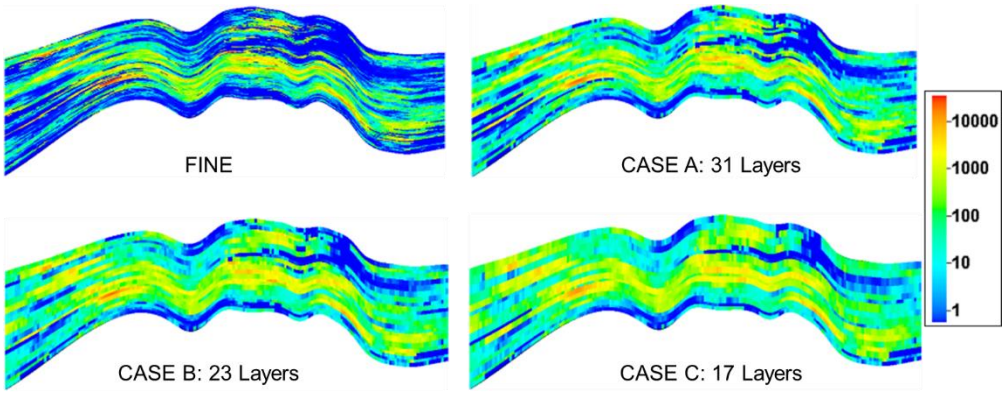

Figure 3.3: Comparsion of fine scale and upscaled PERMX field

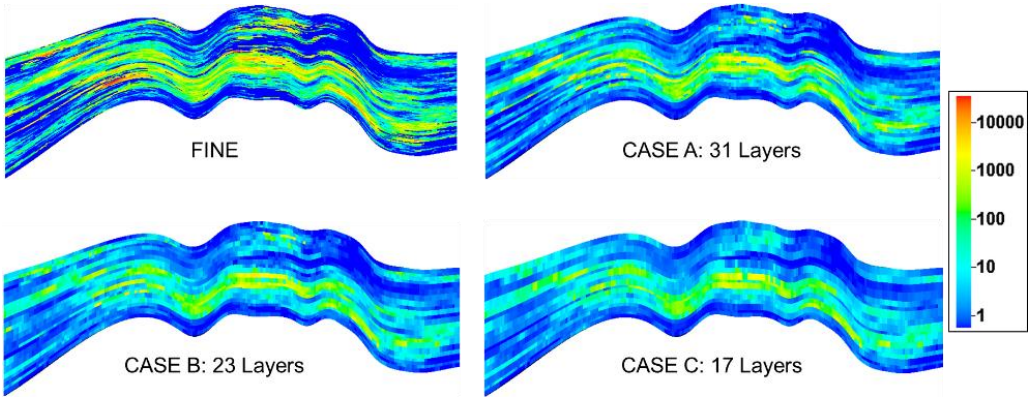

Figure 3.4: Comparsion of fine scale and upscaled PERMZ field

Our upscaling workflow was validated with waterflood simulation using arbitrary repeated five spot well configuration. Streamline-based time-of-flight (TOF) which is defined as travel time of a neural particle along streamline (Datta-Gupta and King, 2007) from injectors and producers, and flow partitions from injectors and producers were visualized and compared at different vertical layer resolutions. TOF from injectors, TOF from producers, flow partitions from injectors (swept volume) and flow partitions from producers (drainage volume) are presented in **Figure 3.5**, **Figure 3.6**, **Figure 3.7**, and **Figure 3.8**. Cell-by-cell TOF comparisons are presented in **Figure 3.9**. The visual are consistent between fine and coarse models validates our upscaling methodology. Further analysis was conducted on the optimal layer coarsening results to compare tracer arrival time distribution at several selected producers across entire reservoir as shown in **Figure 3.11**, **Figure 3.12**, **Figure 3.12**, and **Figure 3.13**.

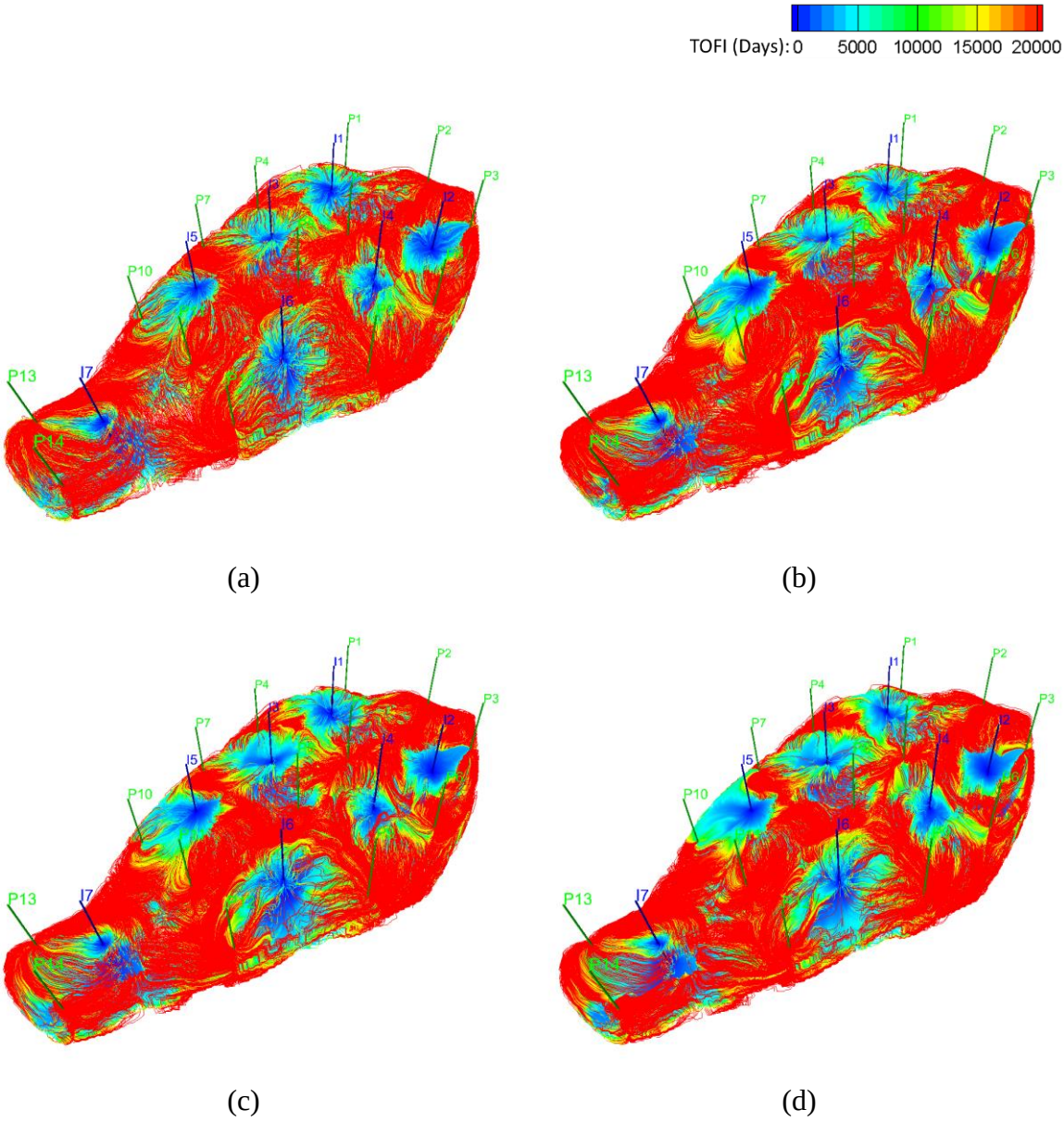

Figure 3.5: Validation of upscaling based on TOF from injector (a) Fine scale (b) 31-layers (c) 23-layers (d) 17-layers

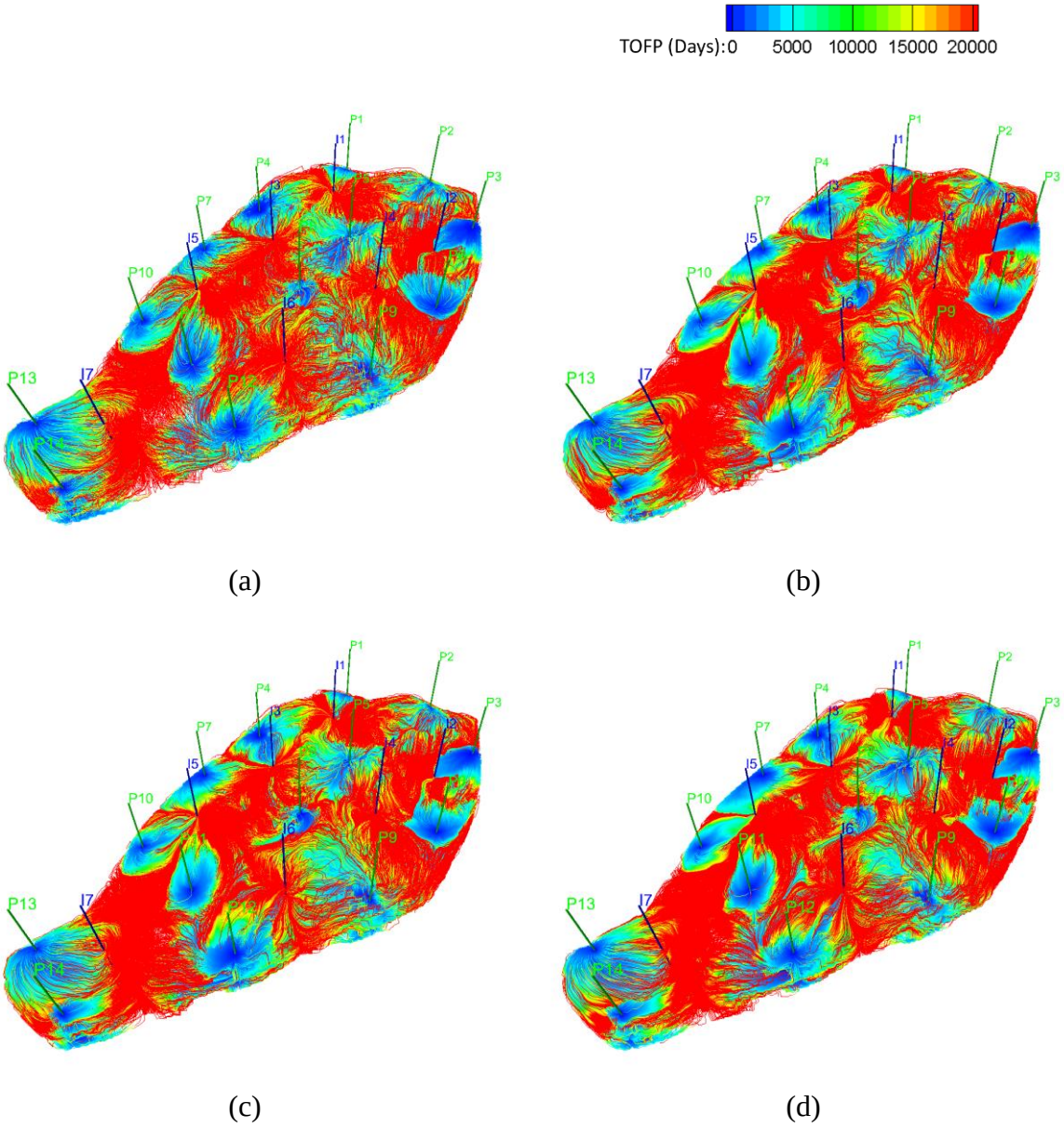

Figure 3.6: Validation of upscaling based on TOF from producer (a) Fine scale (b) 31-layers (c) 23-layers (d) 17-layers

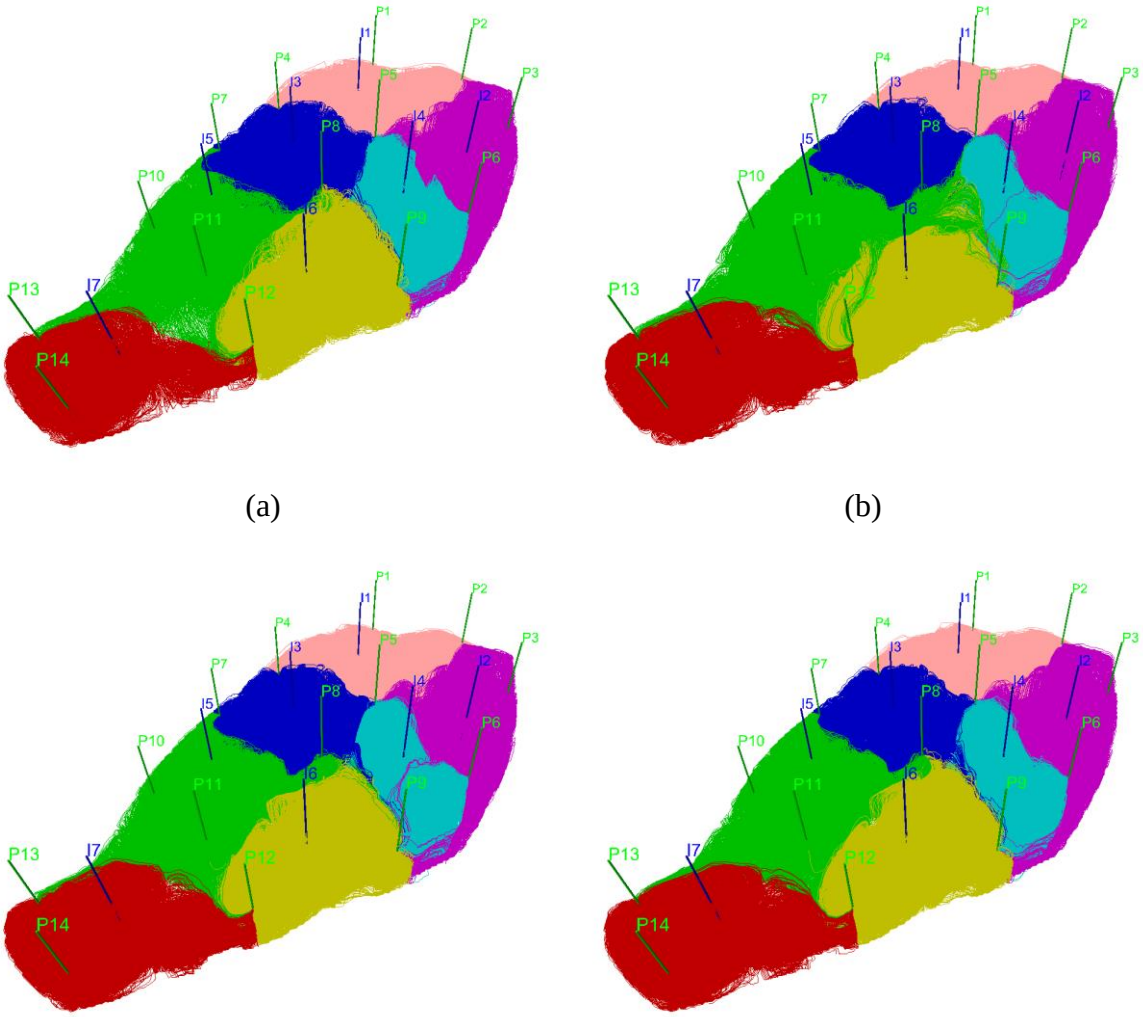

(a) (b)

(c) (d)

Figure 3.7: Validation of upscaling based on flow diagnostics, streamline partitions from injector (a) Fine scale (b) 31-layers (c) 23-layers (d) 17-layers

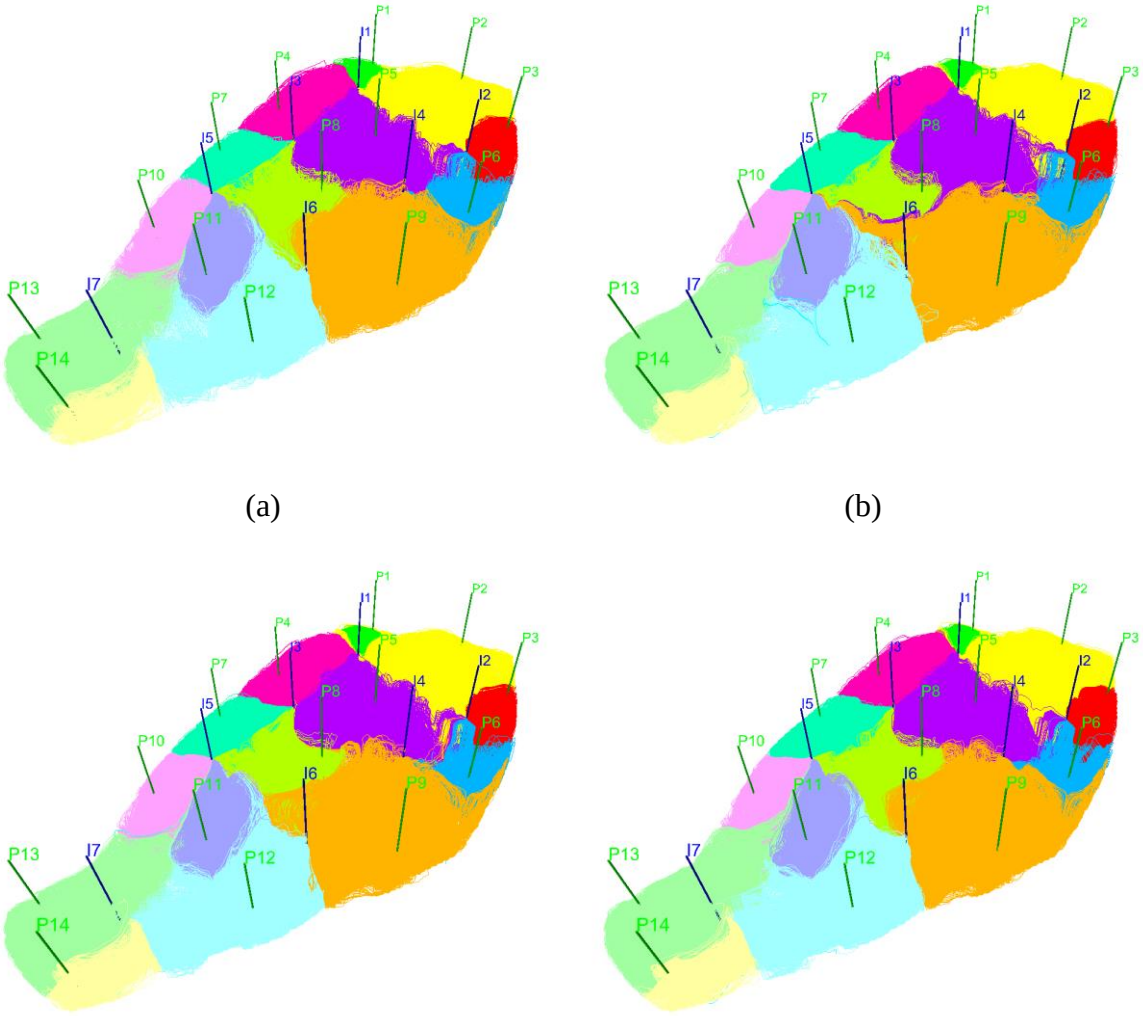

Figure 3.8: Validation of upscaling based on flow diagnostics, streamline partitions from producer (a) Fine scale (b) 31-layers (c) 23-layers (d) 17-layers

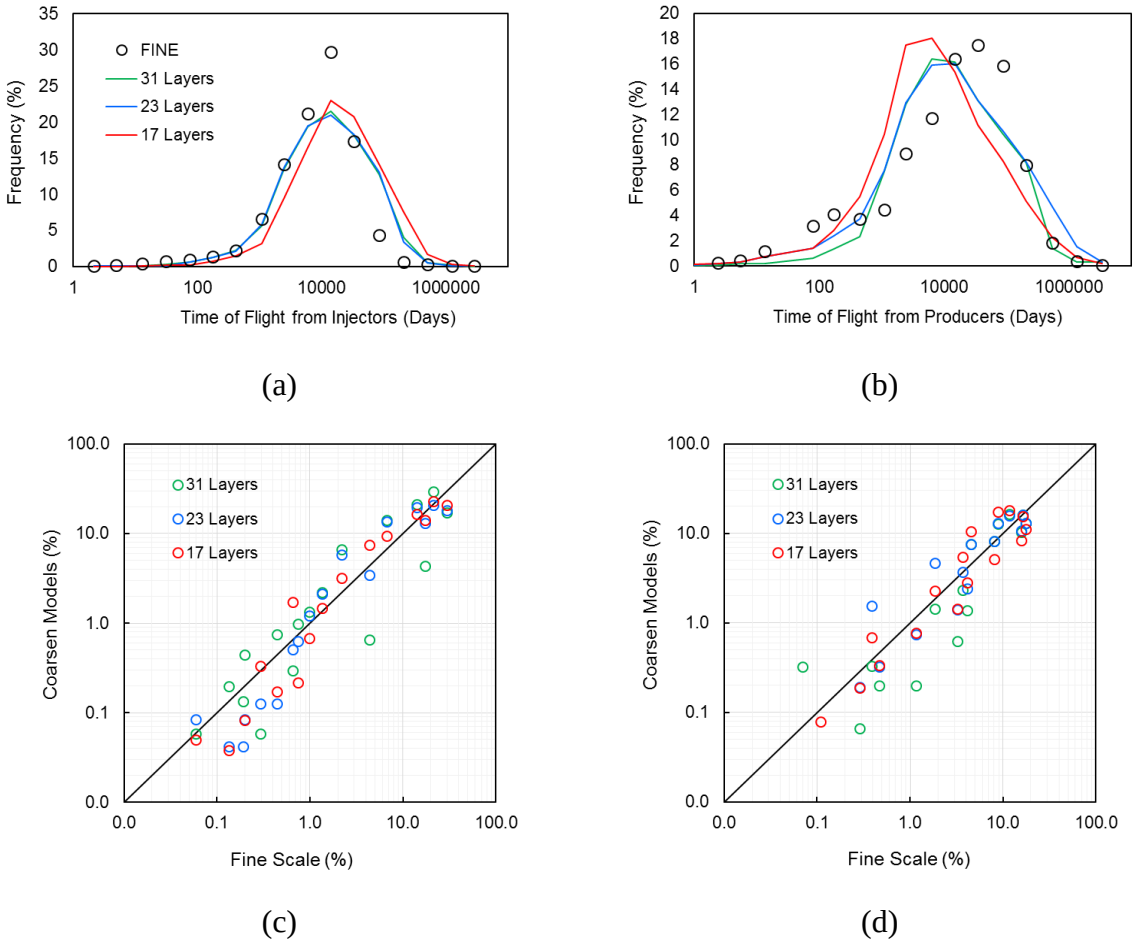

Figure 3.9: Cell-by-Cell TOF comparison (a) TOF from injectors, (b) TOF from producers, (c) QQ-plot (TOF from injectors) and (d) QQ-plot (TOF from producers)

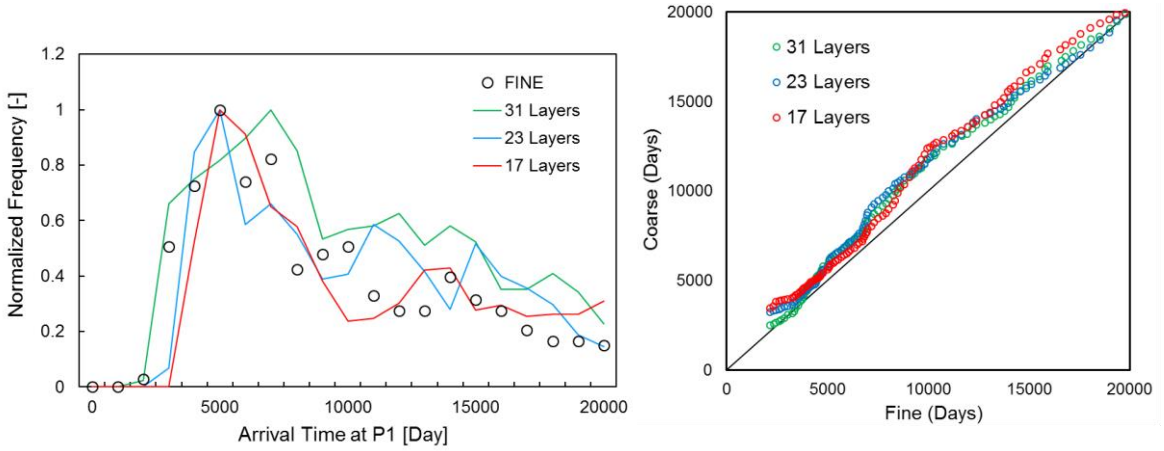

(a) (b)

Figure 3.10: Tracer arrival time distribution comparison at P1 showing (a) density function and (b) direct crossplot

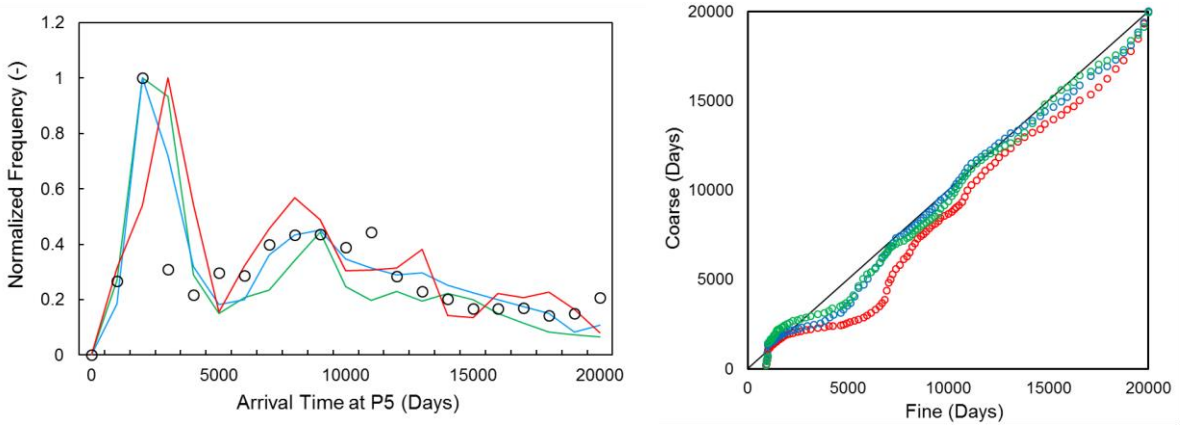

(a) (b)

Figure 3.11: Tracer arrival time distribution comparison at P5 showing (a) density function and (b) direct crossplot

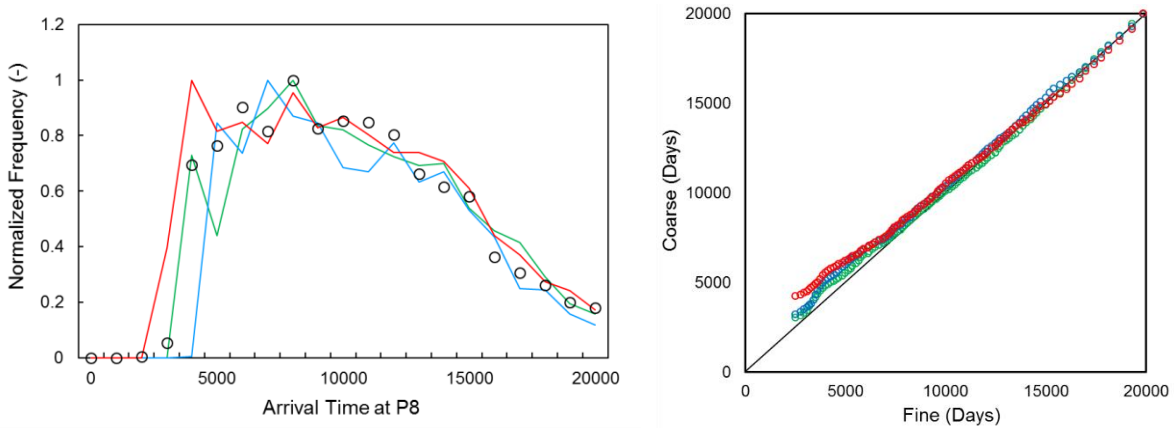

(a) (b)

Figure 3.12: Tracer arrival time distribution comparison at P8 showing (a) density function and (b) direct crossplot

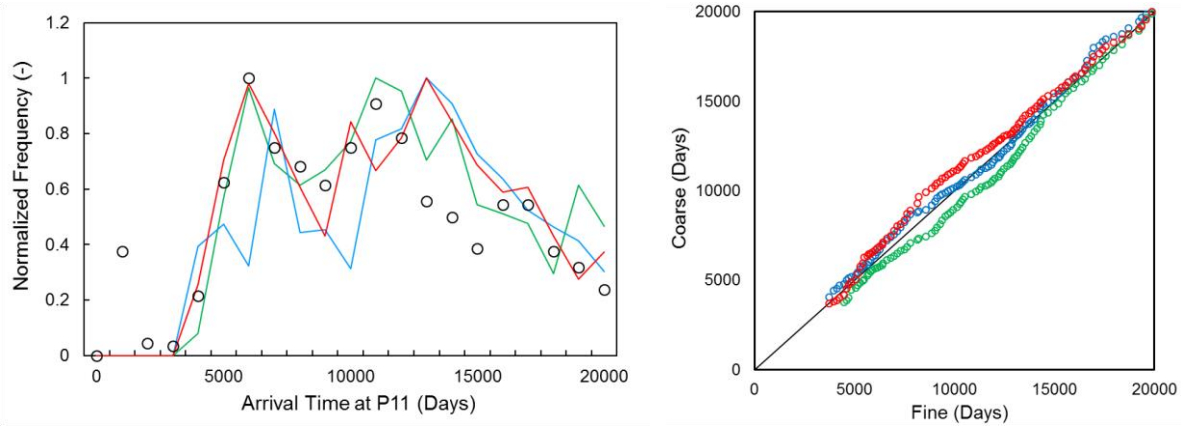

(a) (b)

Figure 3.13: Tracer arrival time distribution comparison at P11 showing (a) density function and (b) direct crossplot

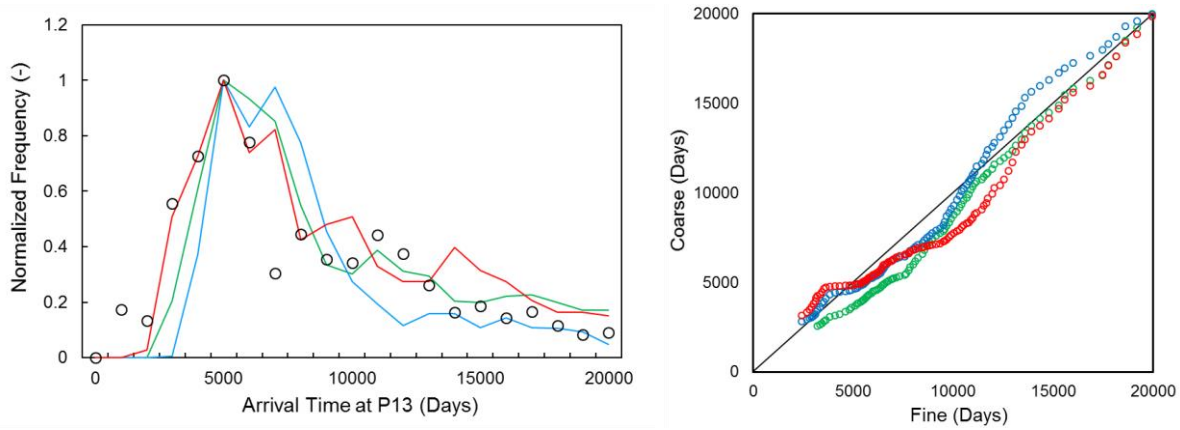

(a) (b)

Figure 3.14: Tracer arrival time distribution comparison at P13 showing (a) density function and (b) direct crossplot

Visual comparisons (**Figure 3.2** - **Figure 3.8**) show good matches between coarsened models and the fine scale model. However, **Figure 3.9** indicates that the 17 layers model shows slightly different results compared to the others. It can also be seen in the tracer arrival time distribution comparisons (**Figure 3.10** - **Figure 3.14**). This can be confirmed by carefully looking at the visual comparisons. For instance, in the cross section view of permeability (**Figure 3.3**), low permeability layers in the left middle are preserved up to the 23 layers model but vanished in the 17 layers model. The 23-layer coarsened model was therefore selected for areal coarsening to further improve on computational efficiency. For our validation tests, we compared the fine scale model with the 3x3x23 and 5x5x23 areal coarsening schemes as illustrated in **Figure 3.15** and **Figure 3.16**. Flow simulation results and computational costs for all coarsened models are compared in **Figure 3.17** and **Figure 3.18**. With our geologic model upscaling, we have successfully reduced the grid cell count by a factor of 100, which resulted in a computational speed up factor of 300 for this waterflood simulation case without

significant loss of accuracy in flow response. The 5x5x23 upscaled model was chosen for the global model calibration discussed in the next section.

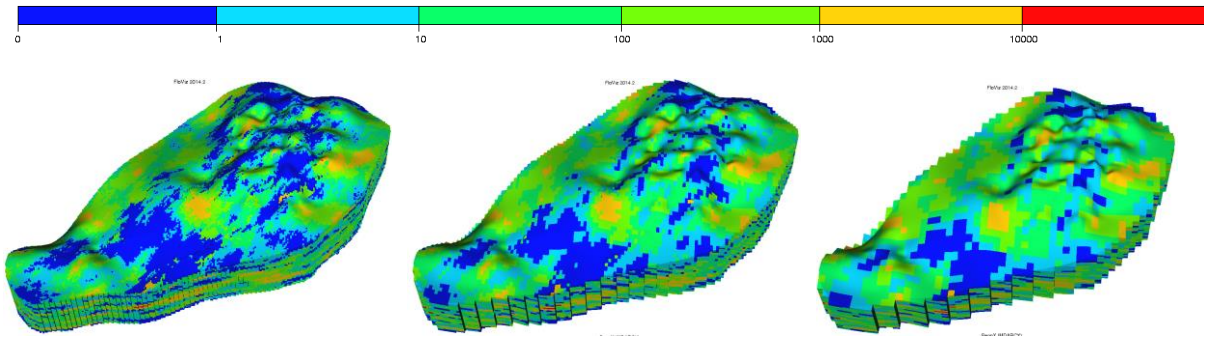

(a) (b) (c)

Figure 3.15: Comparison of upscaled PERMX field (a) 1x1x23, (b) 3x3x23, and (c)5x5x23

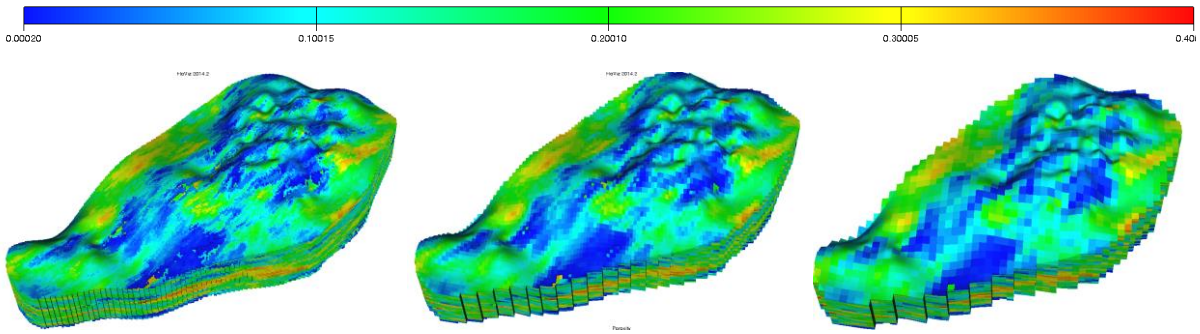

(a) (b) (c)

Figure 3.16: Comparison of upscaled porosity field (a) 1x1x23, (b) 3x3x23, and (c)5x5x23

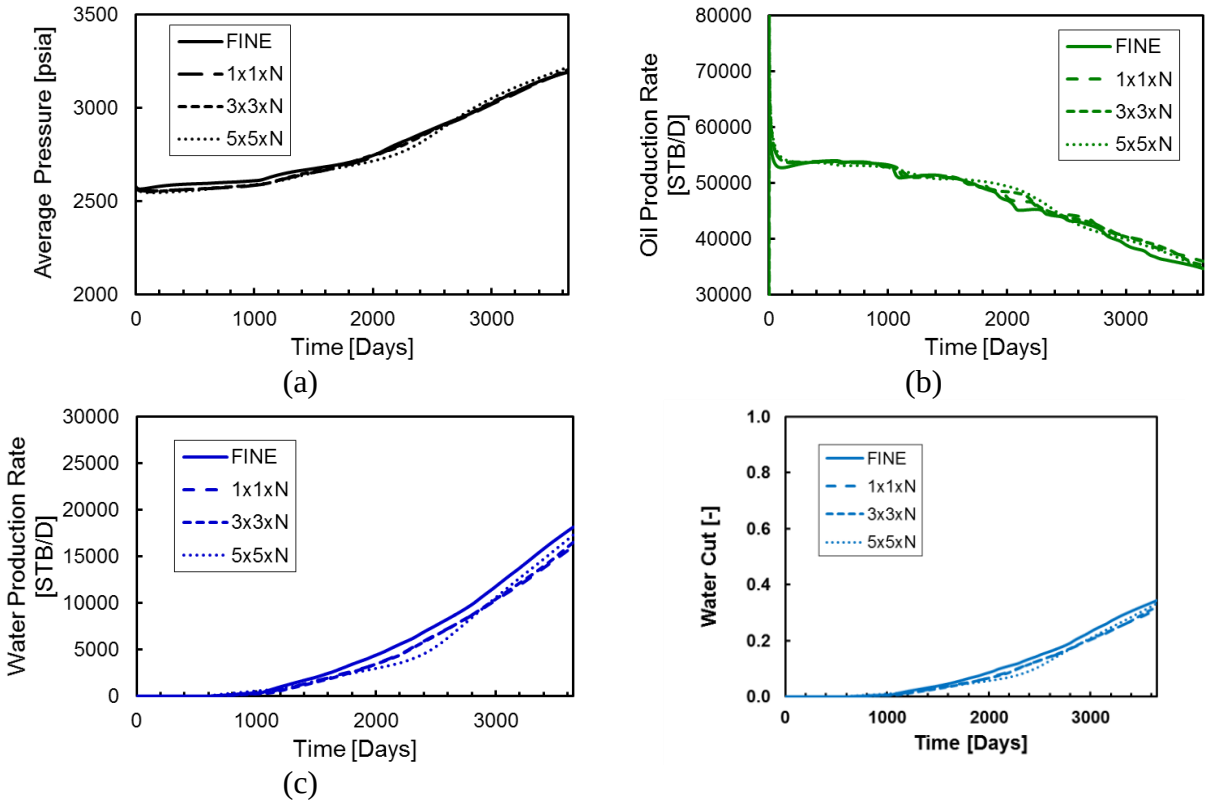

Figure 3.17: Geologic model upscaling validation, comparing simulation responses between fine and coarse models based on (a) average reservoir pressure, (b) oil porduction rate, (c) water production rate, and (d) field water cut metrics

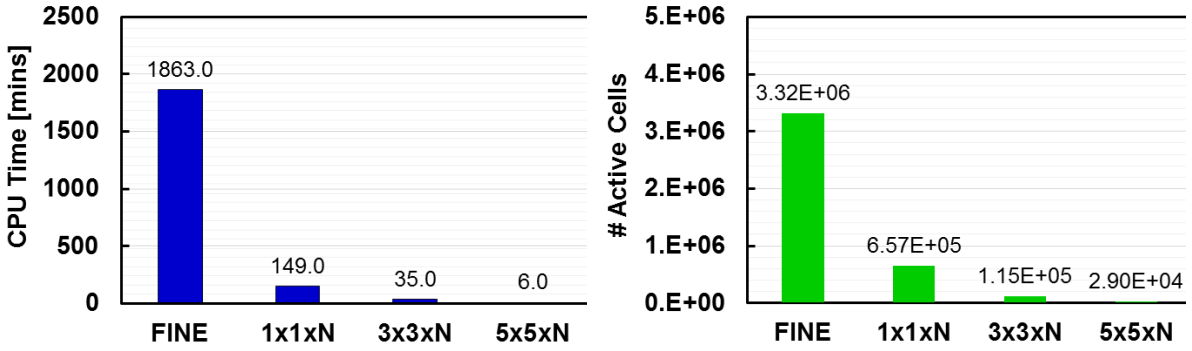

Figure 3.18: Comparison of (a) computational cost and (b) cell count between fine and coarse models

3.3 Model Parameterization and Sensitivity Analysis

The first step is to identify the key performance parameters that characterize the reservoir pressure behavior. The pressure response is primarily impacted by regional pore volume and permeability distribution. For the pore volume calibration, we adopted a spectral clustering technique to partition the model into 5 district regions based on the underlying prior geological and structural features (Kang, et al. 2014). This step begins with the construction of the grid Laplacian defined by Eq. 3.3 where $\mathbf{D}$ represents a diagonal matrix obtained as a row-wise sum of the adjacency matrix $\mathbf{A}$. The elements of the adjacency matrix represent the edge weight between neighboring nodes (grid cells) calculated using Eq. 3.3 and Eq. 3.4 (Bhark, Datta-Gupta and Jarapour 2011):

$$\mathbf{L} = \mathbf{D} - \mathbf{A} \tag{3.3}$$

$$a_{ij} = \exp\left(\frac{-\left\| f_i - f_j \right\|_2^2}{\sigma_P}\right) \times \begin{cases} \exp\left(\dfrac{-\left\| \mathbf{x}_i - \mathbf{x}_j \right\|_2^2}{\sigma_I}\right) & if \left\| \mathbf{x}_i - \mathbf{x}_j \right\|_2 < r \\ 0 & else \end{cases} \tag{3.4}$$

Note that the edge weights a_{ij} incorporates selected grid property values $\left(f_i\right)$ and model structural information in terms of the Euclidean distance $\left(x_i\right)$ between neighboring cell pairs. Hierarchical eigen-decompostion of successive 2nd eigenvectors of the graph results in the graph clusters which define distinct boundaries between regions (Kang, et al. 2014). Using the logarithm of permeability as the grid property in the spectral clustering technique, 5 flow regions were obtained as shown in **Figure 3.19**. Region 1 falls completely out of the hydrocarbon region of the reservoir model. Pore volumes within zones 2 to 5 were perturbed

using constant pore volume multipliers to understand their impact on the pressure depletion of the reservoir.

An increasing trend of the late time average pressure of the reservoir under primary depletion, as observed in **Figure 2.4** suggested significant aquifer influx. Simulation studies by the previous operator suggested stronger bottom water drive compared to edge aquifer drive. The edge aquifer drive is modeled numerically with large pore volume multiplier around the areal boundaries of the reservoir. The bottom 40 layers of the model, containing no hydrocarbons, were coarsened and assigned high pore volume multipliers to represent the bottom aquifer drive.

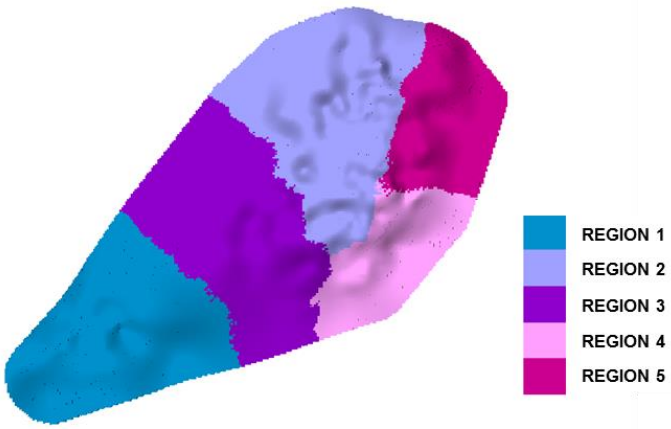

Figure 3.19: Defined regions based on reservoir structure and geology using spectral clustering approach

Based on the well log information characteristic of shale layers in the formation, the reservoir (above of the bottom aquifer) was divided into 4 zones as shown in **Figure 3.20**. Transmissibility multipliers were assigned to inter-zone shale baffles, while vertical permeability anisotropy ratio values (KvKh) were assigned to each of the 4 zones of the formation.

Finally, to account for multiphase flow effects, relative permeability parameters were included in the sensitivity studies. The operator provided a single set of SCAL data containing relative permeability and capillary pressure measurements which were fitted with the Brooks-Corey (Brooks and Corey 1964) and Leverett J-Function (Leverett 1941) models respectively. The three-phase relative permeability functions in **Figure 3.21** were constrained to the provided residual saturation values. Fitted gas phase relative permeability functions were retained due to relatively small free gas flux in the reservoir through the production period, whereas oil-water endpoint as well as exponent values were included in the sensitivity analysis.

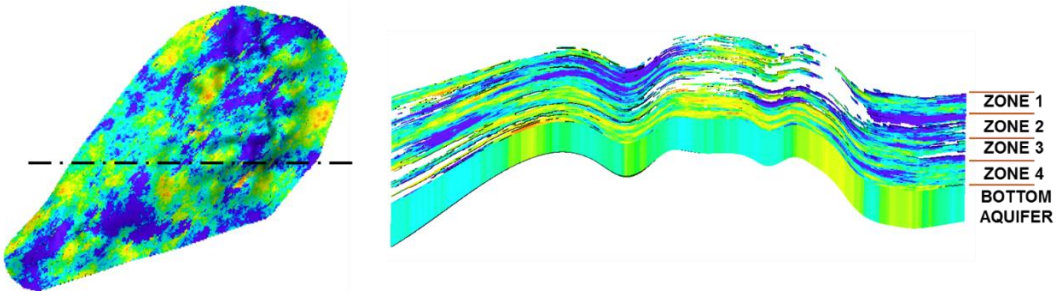

Figure 3.20: Reservoir zone definition based on well log signatures. The model is divided into 4 zones and a bottom aquifer

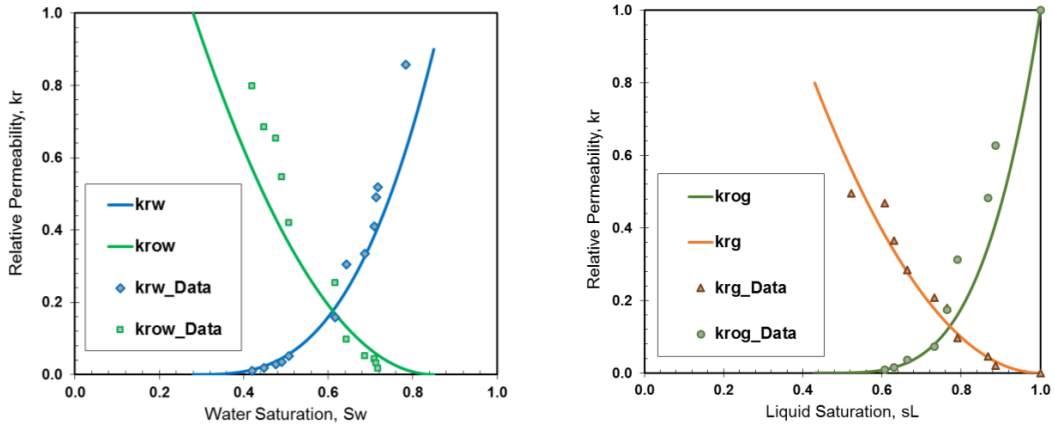

Figure 3.21: Initial three phase relative permability model fitted with provided laboratory data

The list of parameters included in the sensitivity analysis is provided in **Table 3.1**. The table also contains the range of values of each of the parameters used. Note that the KvKh and Z-Transmissibility multipliers are given in base 10 logarithmic values. All flow simulations were conducted by imposing field-wide total liquid withdrawal and injection constraints because reliable well-by-well production data were unavailable. Simulated average reservoir pressure was obtained as the hydrocarbon-pore-volume-weighted field pressure. For all scenarios in the sensitivity analysis, the objective function was computed as:

$$J = \ln\left(\frac{\left\| p_{av,OBS} - p_{av,SIM} \right\|_2}{\sigma_p}\right) + \ln\left(\frac{\left\| FOPT_{OBS} - FOPT_{SIM} \right\|_2}{\sigma_{FOPT}}\right) + \ln\left(\frac{\left\| FLPT_{OBS} - FLPT_{SIM} \right\|_2}{\sigma_{FLPT}}\right) \tag{3.5}$$

Clearly, from the objective function definition, we attempt to match the energy of the reservoir by integrating average reservoir pressure data, fieldwide cumulative oil production (*FOPT*) and liquid production (*FLPT*). Note that the objective function is simply the sum of logarithms of the L2 norms of the fieldwide production and pressure data misfits (between observed and simulated responses), scaled by their respective standard deviations. The relative sensitivity of the i^{th} parameter obtained from the sensitivity study was computed using the dimensionless scaled sensitivities (M. C. Hill 2000) which is the ratio of the change in the objective function to the relative perturbation in the parameter. The dimensionless scaled sensitivity, defined in the following, eliminates disproportionate parameter perturbation sizes and dimensions:

$$sensitivity_i = \frac{\Delta J}{\Delta x_i} x_i^{Base} \tag{3.6}$$

The result of the sensitivity studies is provided in the Tornado chart in **Figure 3.22**, from which it is easy to notice the dominance of the pore volume multiplier for region 2. The other heavy

hitters are the oil relative permeability exponent and the water endpoint relative permeability. It is apparent that the edge aquifer drive shows little or no importance according to the sensitivity studies. Likewise permeability anisotropy ratios for zones 3 and 4 as well as the second and third inter-zone shale barriers have little influence. These were therefore ignored, leaving 12 parameters for the global model calibration. It is interesting to note that KvKh and shale barriers transmissibility values are only important for the top zones. This is a consequence of the fact that all the wells are completed within the oil rim which is mostly contained in the top zone. As a result, high fluid fluxes are concentrated in the top zone throughout the production period.

Table 3.1: List of possible model calibration parameters and their respective assigned bounds

Properties	Parameters	Description	Low	Base	High
Region Pore Volume Multipliers	PVMLT2	Region 2 PV Multiplier	1.0	1.2	1.5
	PVMLT3	Region 3 PV Multiplier	1.0	1.2	1.5
	PVMLT4	Region 4 PV Multiplier	1.0	1.2	1.5
	PVMLT5	Region 5 PV Multiplier	1.0	1.2	1.5
TRANZ Multipliers for Zonal Barriers (log10)	BTTRZMLT	Bottom Aquifer Barrier TRANZ Multiplier	-4.5	-3.5	-2.0
	ZNBARR1	Zone1-Zone2 Barrier TRANZ Multiplier	-3.5	-2.5	-1.5
	ZNBARR2	Zone2-Zone3 Barrier TRANZ Multiplier	-3.5	-2.5	-1.5
	ZNBARR3	Zone3-Zone4 Barrier TRANZ Multiplier	-3.5	-2.5	-1.5
KVKH (log10)	KVKH1	Zone 1 Vertical Permeability Anisotropy Ratio	-2.5	-1.5	-0.5
	KVKH2	Zone 2 Vertical Permeability Anisotropy Ratio	-2.5	-1.5	-0.5
	KVKH3	Zone 3 Vertical Permeability Anisotropy Ratio	-2.5	-1.5	-0.5
	KVKH4	Zone 4 Vertical Permeability Anisotropy Ratio	-2.5	-1.5	-0.5
Aquifer Strength	EAQPVMLT	Edge Aquifer PV Multiplier	1	5	10
	BAQPVMLT	Bottom Aquifer PV Multiplier	30	150	300
Relative Permeability	KROWE	Oil Relative Permeability Exponent	1.0	2.0	3.0
	KRWENDPT	Water Endpoint Relative Permeability	0.2	0.4	1.0
	KRWE	Water Relative Permeability Exponent	2.0	3.0	4.5

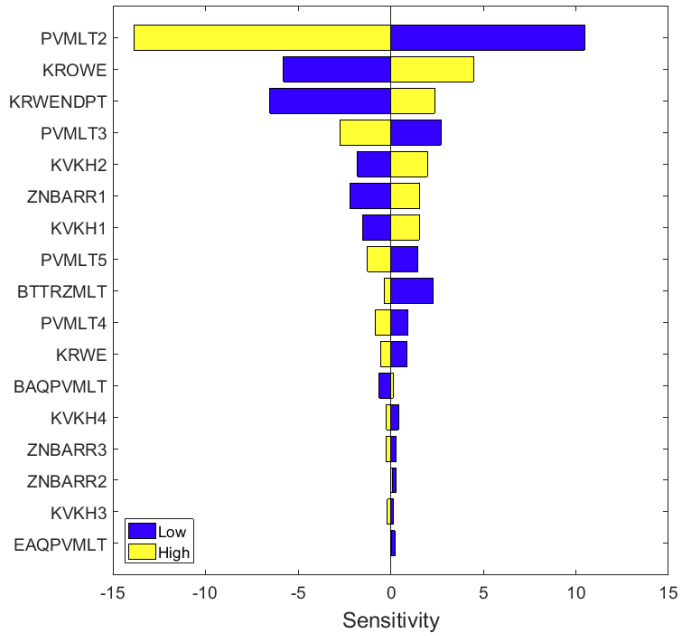

Figure 3.22: Obtained dimensionless scaled sensitivity of model parameters

3.4 Reservoir Energy/Pressure Calibration

Reservoir model calibration was carried out using a Genetic Algorithm (GA) code with an in-built response surface proxy (Lophaven et al., 2002) to update the 12 sensitive global model parameters identified from the sensitivity studies. The objective was to minimize the misfit in the field-wide reservoir fluids production and average field pressure as described in Eq. 3.5, while minimizing the uncertainties in the global parameters. With a population size of 60, a rapid decline of the objective function was achieved within 20 generations (**Figure 3.23 (a)**).

At the same time, a satisfactory reduction in parameter uncertainties was achieved. **Figure 3.23 (b)** shows the comparison between the initial and updated parameter ranges using two sets of overlain box plots. A single boxplot describes the marginal distribution of a parameter. Each boxplot comprises a box, whiskers and the median line. The median line and the top and bottom points of each box respectively denote the 50^{th}, 75^{th} and 25^{th} percentiles of the

represented distribution, while the tips of the whiskers denote the maximum and minimum values of the parameter. From the updated parameter distribution (based on 50 sample realizations), the level of uncertainty reduction is seen to vary with the parameters, with the bottom aquifer barrier showing the highest reduction. The bottom aquifer strength is also fairly well resolved, settling to a median value of about half of the original median. Regional pore volumes were likewise well calibrated, with largest uncertainty reduction observed in region 2 which contains the largest amount of oil in place. Relative permeability parameters, especially the oil relative permeability exponent and endpoint water relative permeability, were also well resolved. **Figure 3.24** compares the oil-water relative permeability functions, fractional flow curves, and mobility curves of all calibrated ensembles overlain on a set of laboratory data based on a single core from the reservoir. Clearly, the calibration results capture the main trend of relative permeabilities in the reservoir.

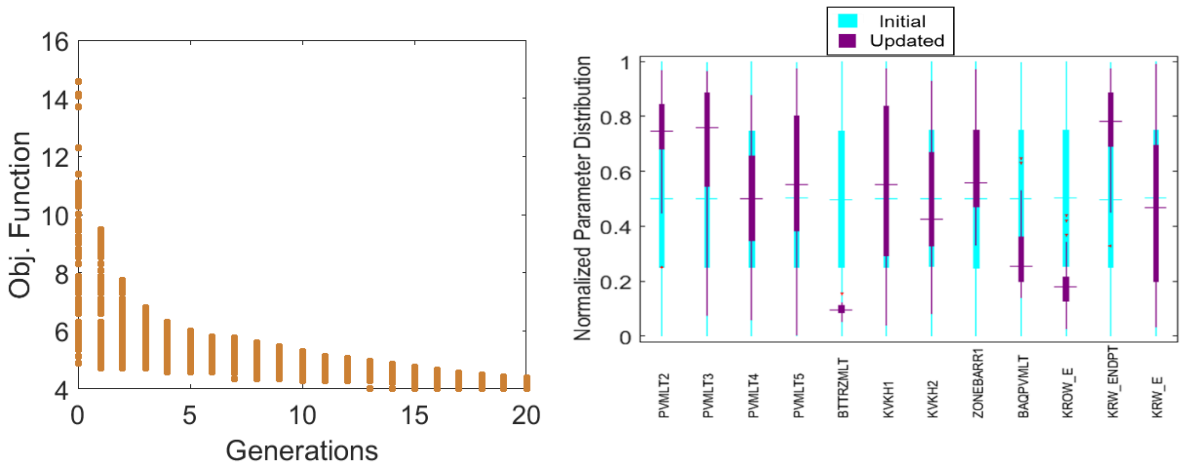

(a) (b)

Figure 3.23: (a) A plot of objective function reduction with generation during GA runs. (b) Box plots of prior and updated model realizations showing general reductino in parameter uncertainties

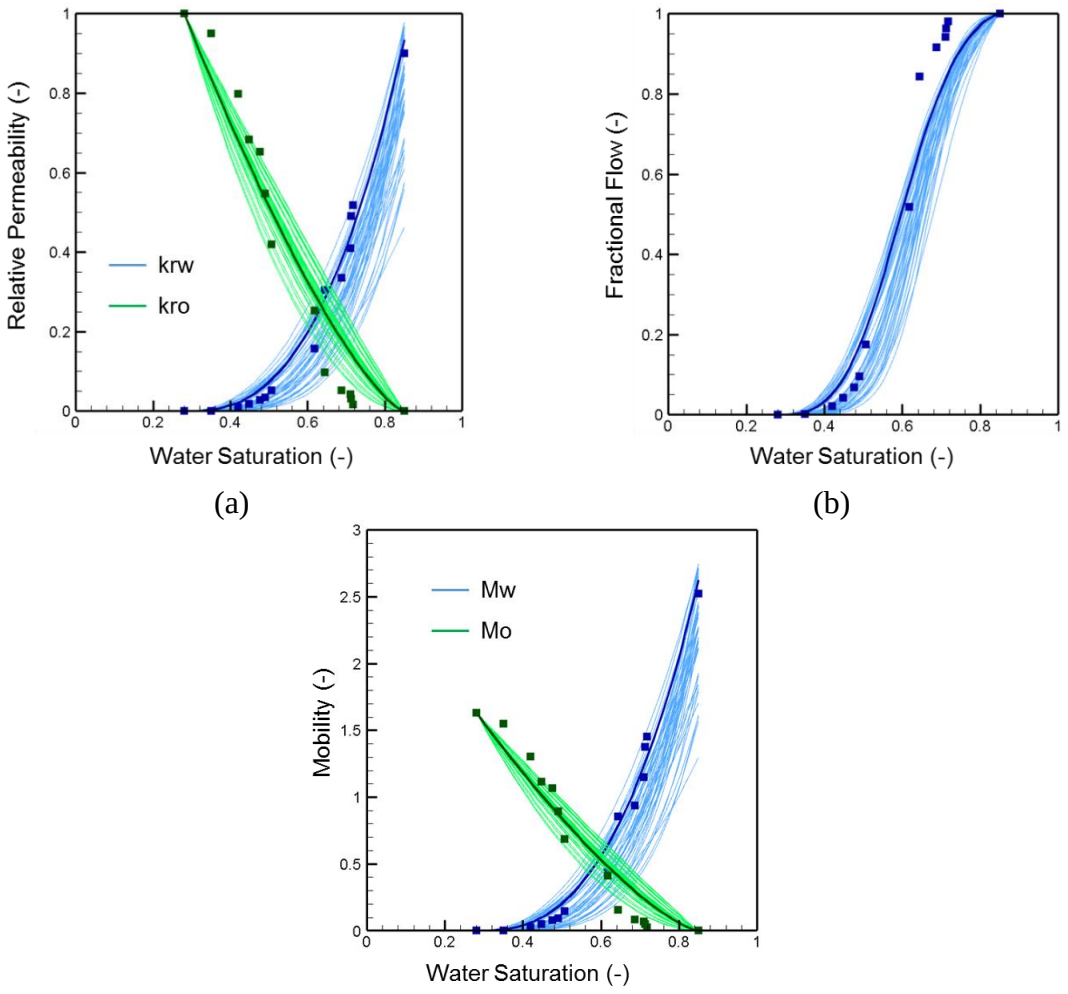

Figure 3.24: Oil-water relative permeability functions of ensemble of updated models, compared with laboratory data. Model seleted for permeability field update captures the general trend in the data

Calibrated model responses are displayed with the field production data in **Figure 3.25**. Field-wide liquid production and water production responses show relatively smaller spreads, compared to the average field pressure response, since all simulations are constrained by the total liquid production rate. All calibrated models capture the characteristic decline in average pressure due to liquid withdrawals under primary depletion which lasted over 30 years. The brief rise in reservoir pressure due to water injection between 1971 and 1980, the following

pressure decline and the final consistent rise in average pressure (due to bottom aquifer influx) were all captured within the model response spread. This goes further to validate the quality of the calibrated models in capturing the interplay between different drive mechanisms in the reservoir.

Available bottomhole pressure and cumulative water production data of a few wells were also compared with the calibrated model responses as shown in **Figure 3.26**. It worth mentioning here that the objective function in Eq. 3.5 does not include the data misfit from these wells. Nevertheless, an acceptable agreement between the calibrated models and the individual well production data can be observed, except for wells in region 3 which show slight discrepancies. Another interesting and important deduction from this observation is that the reservoir is highly connected hydraulically. In other words, isolated flow units are unlikely in this formation since a match of the global average pressure resulted in local matches of available well BHP data.

Going back to the field-wide model responses, a minor bias in field water production across all model samples can be observed in the first 25 years of production. This is due to the lack of consistent production data during this period. Again, due to unavailability of well-by-well production data, it was difficult to accurately capture the steep rise in oil production during the water injection period (1971 to 1980). This seeming inadequacy of the calibrated models in this regard also suggests the need for a global update of the reservoir permeability field.

Although not presented here, our next step is to calibrate recent water injection data provided from the operator. The results obtained here serve as the starting reservoir model for the permeability update discussed in detail in the next section. The objective for the permeability update will be to integrate bottomhole pressure data from two observation wells

and flowing bottomhole pressure data from several injection wells during a 6-month water and CO_2 injection period. In preparation for this step, we ranked the ensemble of models obtained from the global energy balance based on their fit to the available injection data. This is for the benefit of a robust model calibration which requires modest changes in the permeability field. The selected model responses are shown in **Figure 3.25**, and the corresponding parameters shown in **Table 3.2**. For visual comparison, relative permeability function of the selected model realization is also overlain on the plot in **Figure 3.24**, showing acceptable agreement with the provided SCAL data.

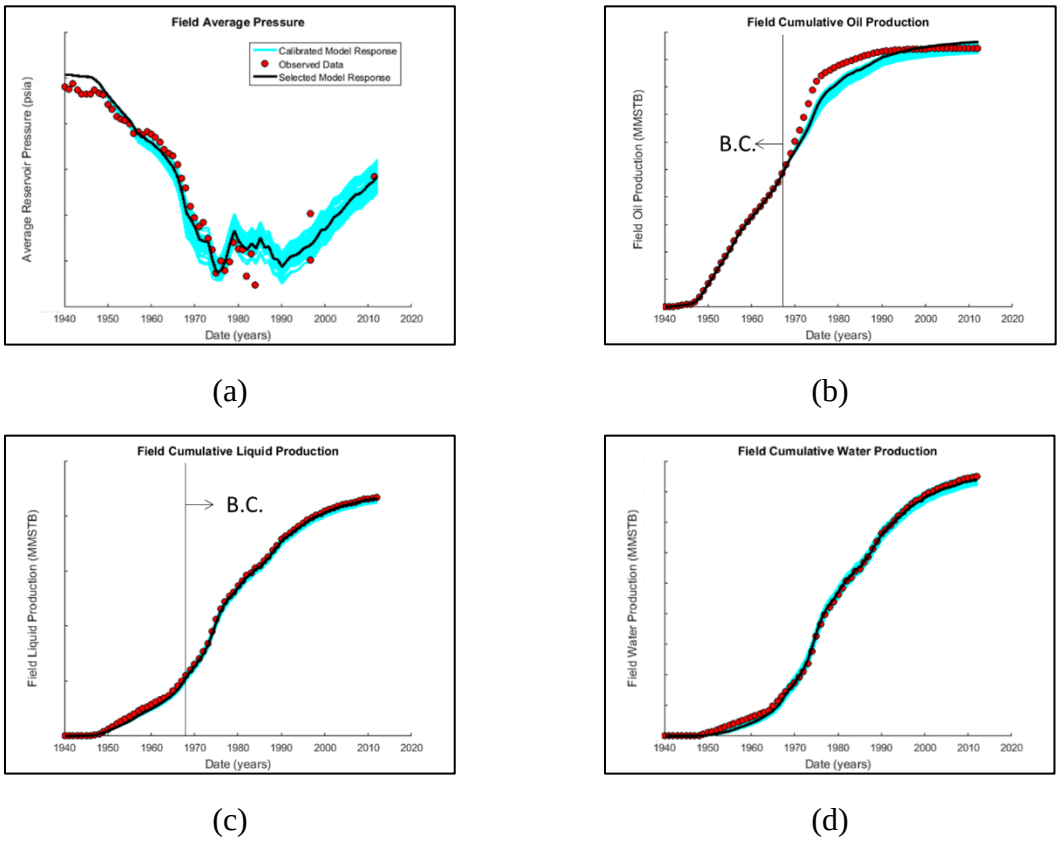

Figure 3.25: Calibrated model responses compared with historical data

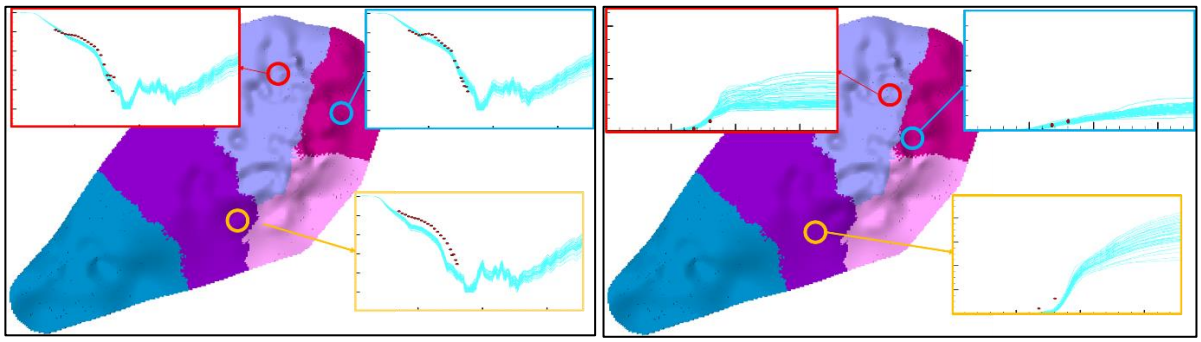

(a) (b)

Figure 3.26: Well by well model calibration validation based on (a) Bottomhole flowing pressure and (b) cumulative water production of available well data. Location of wells are indicated on the regions map

Table 3.2: Representative model parameter values used for permeability model update

Parameter	Value	Parameter	Value	Parameter	Value
PVMLT2	1.466	BTTRZMLT	-4.286	BAQPVMLT	114
PVMLT3	1.393	ZNBARR1	-2.721	KROWE	1.36
PVMLT4	1.188	KVKH1	-1.153	KRWENDPT	0.93
PVMLT5	1.343	KVKH2	-0.472	KRWE	2.67

CHAPTER IV

DEVELOPMENT AND VALIDATION OF THE EMBEDDED DISCRETE FRACTURE MODEL

4.1 Chapter Summary

A significant percentage of hydrocarbon reserves are trapped in fractured media. The development of fracture modeling approaches are therefore an active field of research. A widely used method is multiple continuum approaches. Although computationally efficient, these approaches are likely to be limited to capture detailed flow mechanisms in complex fracture media due to non-physical abstractions inherent in simplifications in the formulations. In recent years, the unstructured discrete fracture model (USDFM) approach has grown as a more accurate alternative for fracture modeling in which no simplifications are made. High resolution unstructured gridding is necessary to describe fracture and matrix in the same domain, and therefore, these models are computationally prohibitive. Recently presented, the embedded discrete fracture model (EDFM) is essentially in-between multiple continuum models and USDFMs. A structured grid is used for matrix domain, whereas fractures are explicitly placed within the matrix domain. Matrix-fracture interactions are described by a local flow assumption with a single transmissibility. EDFM can circumvent drawbacks in conventional approaches while maintaining advantages of them. We present development and validations of the EDFM.

4.2 Literature Review

Naturally fractured reservoirs (NFRs) account for a significant portion of the world's remaining energy resources (Allan and Sun 2003). More than 60 percent of the world's proven oil reserves and more than the 40 percent of world's gas reserves are in fractured media (Schlumberger 2008). In addition, because of the advent of the hydraulic fracturing and horizontal well, unconventional reservoirs are now important resources in the United States. However, it is often challenging to characterize complex fracture distributions due to complex fracture geometry, high conductivity and high uncertainties. For instance, the presence of highly conductive fracture pathways can cause premature breakthrough of injected fluids in NFRs which result in poor hydrocarbon recovery (Hui, et al. 2017). Modeling and careful reservoir management are therefore important to efficiently develop fractured media (Moridis and Freeman 2013).

Many fracture modeling approaches have been presented. A widely used approach is the dual porosity approach (Warren and Root 1963), which discretizes a reservoir into two domains, matrix and fracture. Main flow paths occur in the fracture domain whereas the matrix domain serves as source/sink of a corresponding fracture gridblock. Matrix-fracture interactions are described by the transfer function which is proportional to a geometrical shape factor, and the driving force is the pressure drop between a matrix gridblock and surrounding fractures. The dual porosity approach was originally limited to a single phase and later extended to multiphase flow in NFRs (Kazemi, L.S. Merrill and Zeman 1976). In the dual porosity approach, matrix-matrix connections are assumed to be negligible. Dual porosity-dual permeability (DPDP) approach that accounts for matrix-matrix connections has therefore been

developed (Blaskovich, et al. 1983, Hill and Thomas 1985, Dean and Lo 1988). Although computationally efficient, it is well recognized that dual continuum approaches have limitations due to simplifying assumptions. Dual continuum approaches are originally designed for situations where fractures are densely distributed and well connected which may not be valid in reality. It is proven that these approaches can lose accuracy when fractures are disconnected or a small number of large-scale fractures dominate the flow (Moinfar, et al. 2011). Moreover, the use of dual continuum approaches in unconventional reservoirs could result in inaccuracy, because it may take several years to reach the pseudo-steady state in the ultra-tight matrix system (Jiang and Younis 2016). Multiple Interacting Continua (MINC) (Pruess and Narashiman 1985) allows the accurate description of fluid flow with steep gradients at the matrix-fracture interfaces by appropriate subgridding of the matrix gridblocks (Moridis and Freeman 2013) and therefore the MINC is suitable for tight media. However, the continuous representations can be problematic for fracture networks with sparse and irregular spacing.

The unstructured discrete fracture model (USDFM) approach has been proposed as a more accurate alternative for fracture modeling (Noorishad and Mehran 1982, Monteagudo and Firoozabadi 2004, Hyman, et al. 2016). USDFM represents fractures and a matrix in the same domain using detailed unstructured grids without any simplifications in geometry which allow accurate computations compared to dual-continuum approaches. However, USDFM is often computationally expensive due to high resolution gridblocks surrounding fractures. This issue has been improved by state-of-the-art linear solvers (Hui, et al. 2013) and massively parallel codes (Hyman, et al. 2016). However, it is still computationally too expensive to run

a large number of simulations on USDFM for history matching, optimization, or uncertainty quantification purposes which usually require hundreds of simulations. Generating detailed unstructured mesh is another challenge in USDFM.

The embedded discrete fracture model (EDFM) is essentially in-between multiple continuum models and the USDFM (Li and Lee 2008, Moinfar, et al. 2014). A Cartesian grid may be used for matrix domain, whereas fractures are explicitly placed within the matrix domain as 2D planes. Matrix-fracture interactions are described by a local flow assumption with a single transmissibility. The EDFM can circumvent drawbacks in conventional approaches while maintaining advantages of them and therefore it has been an active area of research in recent years as an alternative approach to conventional fracture modeling techniques. The EDFM was initiated by Li and Lee (2008) and improved by Moinfar, et al. (2014). Filho, J. S. A. Shakiba and Sephehrnoori (2015) developed a preprocessor for general transport index calculations. Jiang and Younis (2016) presented the hybrid model that they couple EDFM with MINC. Later, the EDFM is extended for non-planar, irregular fracture shapes (Xu, et al. 2017). The EDFM can lose accuracy when matrix gridblocks are aggressively coarsened or strong pressure and/or saturation gradients exist within a matrix gridblock (Moinfar, et al. 2014, Hui, et al. 2017). In order to address this limitation, Tene, et al. 2017 proposed the projection-based EDFM (pEDFM) that represents matrix-fracture interactions more generally and is similar to USDFM. Several applications have been presented. Panifili and Cominelli (2014) applied the EDFM for an EOR processes in real fractured reservoirs and confirmed capability of the EDFM. Chai et al., (2016) applied the EDFM for history matching using Markov-Chain Monte Carlo (MCMC).

In this study, we present development of the EDFM following Moinfar, et al. (2014). Our approach is to develop preprocessing codes and couple them with a commercial simulator, ECLIPSE so that we will be able to apply the developed EDFM to practical applications. The developed model has been validated comparing against fine scale explicit fracture cases including NFRs and unconventional reservoirs.

4.3 Methods

We have implemented the EDFM presented by Li and Lee (2008) and Moinfar, et al (2014) in a commercial simulator ECLIPSE (Schlumberger 2014). This section presents mathematical formulations and the implementation of the EDFM. As mentioned, concepts in the EDFM are similar to dual-continuum models in which main flow paths occur in the fracture domain and each fracture gridblock has a matrix gridblock as a source/sink i.e., the number of elements in the fracture domain and the matrix domain are, therefore the same. On the other hand, in the EDFM, fractures are explicitly described in a separate computational domain as two-dimensional planes in addition to the matrix domain as illustrated in **Figure 4.1**. These fractures are discretized by the cell boundaries in the matrix domain. The fracture gridblocks are then linked with corresponding matrix gridblocks via non-neighbor connections (NNCs) which define additional connections between any gridblocks in finite-difference/volume framework (**Figure 4.2**) and is based on a previously presented approach in DFM (Karimi-Fard, Durlofsky and Aziz 2004).

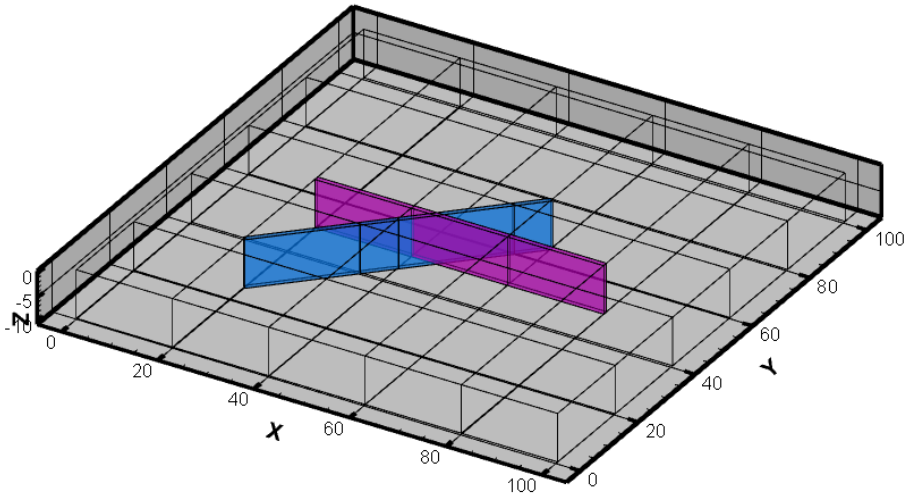

Figure 4.1: An illustration of the EDFM

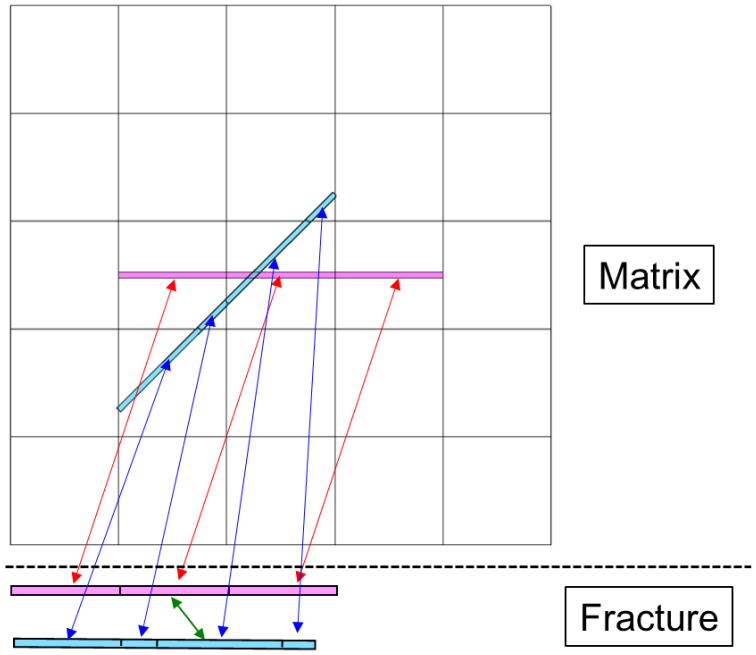

Figure 4.2: Discretization and NNCs in the EDFM.

The general form of the governing equation of the EDFM is given by:

$$\sum_{j=o,w,g}^{n_p}\left[\frac{\partial}{\partial t}\left(\phi y_{ij}\rho_j S_j\right)+\nabla\bullet\left(y_{ij}\rho_j\vec{u}_j\right)-y_{ij}\tilde{q}_j\right]+q^{NNC}=0 \tag{4.1}$$

where, ϕ is the porosity, y_{ij} is the phase mole fraction of component *i* in phase *j*, ρ_α is the molar density of phase α, S_α is the saturation of phase α, $\vec{u}_j$ is the velocity of phase α, and q_i is molar rate of component *i* in phase *j*. The q^{NNC} term is to describe the fractures:

$$q^{NNC}=\sum_{m=1}^{n_{NNC}}A_m^{NNC}\sum_{j=1}^{n_p}\frac{k_m^{NNC}k_{rj}}{\mu_j}y_{ij}\rho_j\left[\frac{\left(p_j-\gamma_j D\right)-\left(p_j-\gamma_j D\right)_m^{NNC}}{d_m^{NNC}}\right] \tag{4.2}$$

where, n_{NNC} is the number of NNCs for a gridblock, A_m^{NNC} is the area open to flow, k_m^{NNC} is the harmonic average of permeability, k_{rj} is the relative permeability, μ_j is the viscosity, p_j is the pressure of phase *j*, γ_j is the specific gravity of phase *j*, d_m^{NNC} is the average normal distance. Note that the EDFM can also be used in a black oil model. A key concept in the EDFM formulations is the transmissibility, also called transport index (TI) in the Eq. (4.2), $A_m^{NNC}k_m^{NNC}/d^{NNC}$ varying according to geometrical interactions between a fracture gridblock and its neighboring matrix. There are three types of TI which are used to describe interactions of matrix-fracture and fracture-fracture via NNCs. **Figure 4.3** presents a summary of these NNCs.

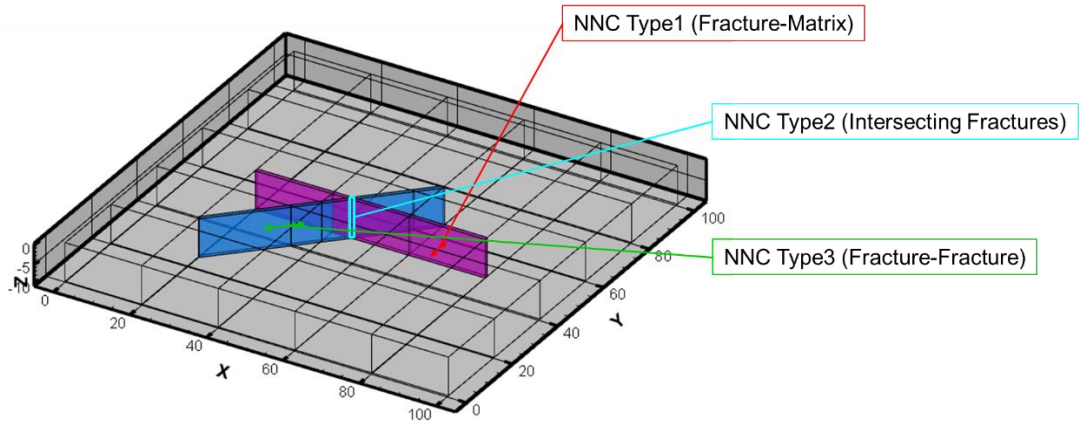

Figure 4.3: An illustration of intersecting fractures

(i) Matrix-fracture

As mentioned, the matrix-fracture TI is described by

$$TI = \frac{A_m^{NNC} k^{NNC}}{d_m^{NNC}} \tag{4.3}$$

where, A_m^{NNC} is the surface area of the fracture, k^{NNC} is harmonic mean of the matrix and fracture permeability, and d_m^{NNC} is the average normal distance. Eq. (4.3) is based on an assumption that pressure gradient between a matrix gridblock and a fracture gridblock is linearly distributed (Li and Lee 2008). **Figure 4.4** presents a simple case of the EDFM in which fractures are assumed to be fully penetrated in the vertical direction. Pressure in a matrix gridblock with a fracture is assumed to be an average pressure. If a fracture is not fully penetrated in a gridblock, we first extend a fracture such as if it is fully penetrated. Then, compute the actual TI assuming that the transmissibility is linearly proportional to surface area of the fracture in the gridblock.

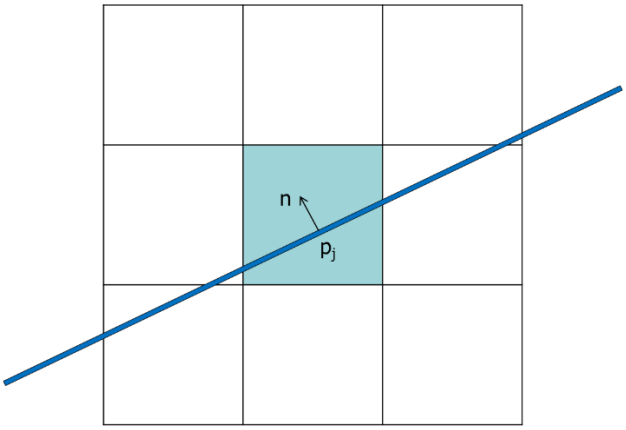

Figure 4.4: A schematic of a matrix gridblock that contains a fracture

We can therefore define the average normal distance from a fracture to the neighboring matrix gridblock:

$$d_m^{NNC} = \langle d \rangle = \frac{\int_V x_n dV}{V} \tag{4.3}$$

where, dV, x_n, and V are the differential volume element, the normal distance from the fracture and volume of a gridblock. Although analytical solutions are available in simple geometries, it can be difficult to generalize in practical applications. Hence, we numerically computed the volume integral in Eq. 4.3.

(ii) Intersecting fractures

We applied the same approach presented by (Karimi-Fard, Durlofsky and Aziz 2004). In this approach, TI is given by

$$TI = \frac{T_1 T_2}{T_1 + T_2} \tag{4.4}$$

And,

$$T_i = \frac{k_{fi}\omega_{fi}L}{f_{fi}} \tag{4.5}$$

where, k_{fi} is the fracture permeability at gridblock *i*, ω_{fi} is the fracture aperture at fracture *i*, *L* is the length of the intersection line bounded in a gridblock, and d_{fi} is the average normal distance from the center of the fracture sebsegments.

(iii) Fracture-fracture

As illustrated in **Figure 4.3**, this type of NNCs are for connections within a fracture. We also apply Eq. (4.3). k_m^{NNC} is equal to harmonic mean of adjacent fracture gridblocks, A_m^{NNC} is the surface area between the two gridblocks i.e., aperture times cell height if a fracture is vertically penetrated, and d_m^{NNC} is the distance between the centers between the two gridblocks.

We have implemented the EDFM approach in ECLIPSE. Specifically, we developed a preprocessing code which compute TI based on geometry and properties of matrix and fracture. The preprocessing codes generate additional control volumes to describe fractures. The fracture gridblocks and adjacent matrix gridblocks will then be liked through NNCs using NNC keyword in ECLIPSE (Schlumberger 2014). Detailed input and output are described in **Appendix A**.

4.4 Validation

This section presents validations of implementation of the EDFM. Five cases including three cases for NFRs based on a previous study (Moinfar, et al. 2014) and two cases for unconventional reservoirs will be demonstrated. The EDFM solutions are compared with fine

scale explicit fracture cases. Prior to conducting these validations, we first validated the implementation of the q^{NNC} term, i.e., average normal distance and TI calculations which can be found in **Appendix B**.

Case 1: Water floods in a 2D reservoir with aligned fractures

This example is to confirm accuracy of the EDFM with a typical secondary recovery scenario in NFRs. The model is discretized into $30 \times 15 \times 1$ with cell sizes of $20.0 \times 20.0 \times 15.0$ (ft). Two fractures are vertically penetrated and aligned with coordinate axes (**Figure 4.5**). Brief descriptions of other reservoir properties are provided in **Table 4.1**. The fluids are described by a black oil model including aqueous and organic phases and assumed to be an isothermal system. Two phase relative permeability curves in the matrix domain and the fracture domain are presented in **Figure 4.6**. Capillary pressures are assumed to be negligible for simplicity. We applied commonly used the straight-line relative permeability curves for the fracture domain. The model consists of a single injection well and a single production well. Wells and boundary conditions are provided in **Figure 4.5**. **Figure 4.7** and **Figure 4.8** present the comparison of pressure distribution and aqueous saturation distributions between the EDFM and the reference solution with explicit fractures in which we defined fractures using tartan grids. In addition, comparison of water cut is shown in **Figure 4.9**. Computed water cut by the EDFM shows good agreement with the reference solution. Further, **Figure 4.10** compares CPU time between the reference solution and the EDFM. We can see slight improvement in computational efficiency in the EDFM approach but not significant with this simple example.

Table 4.1: Reservoir Properties of the Case 1

Parameter	Values
Matrix	
Permeability, mD	20.0
Porosity	0.10
Fracture	
Permeability, mD	7.00e+05
Porosity	0.010
Aperture, ft	0.0264

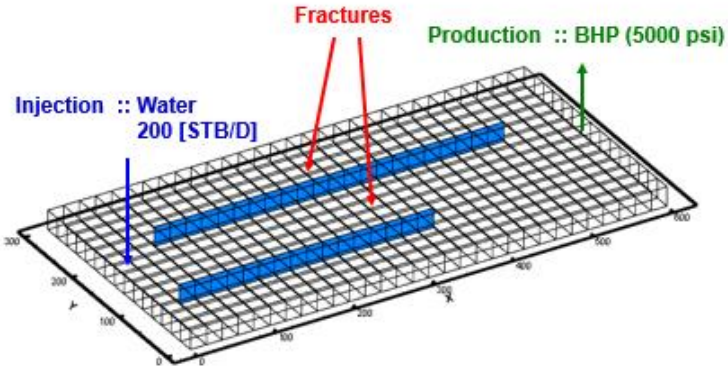

Figure 4.5. Schematic of the 2D aligned fractures

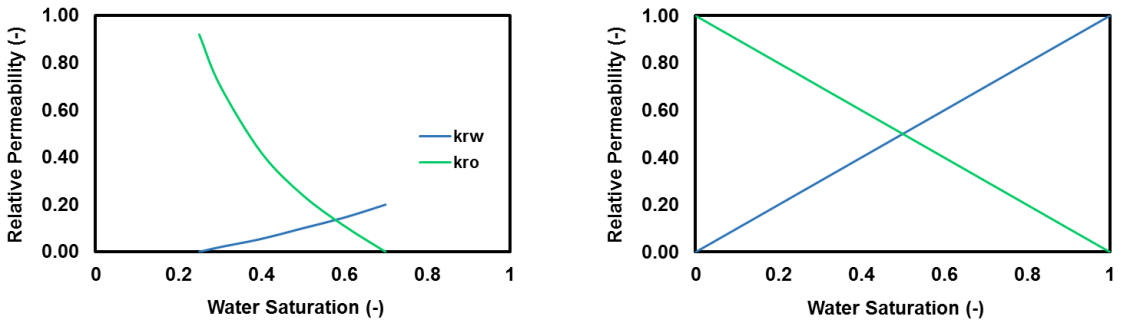

(a) (b)

Figure 4.6: Two phase relative permeability curves in matrix and fracture (a) matrix and (b) fracture

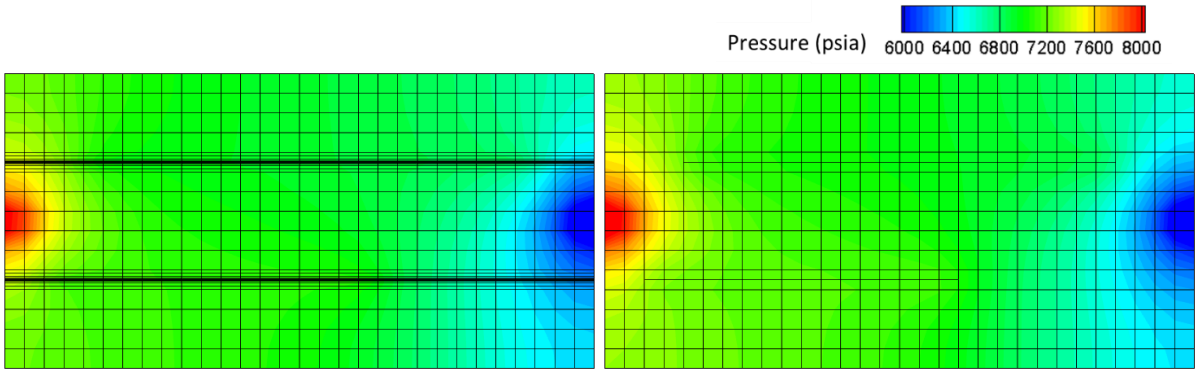

Figure 4.7. Pressure distribution comparison: (a) Reference solution and (b) EDFM

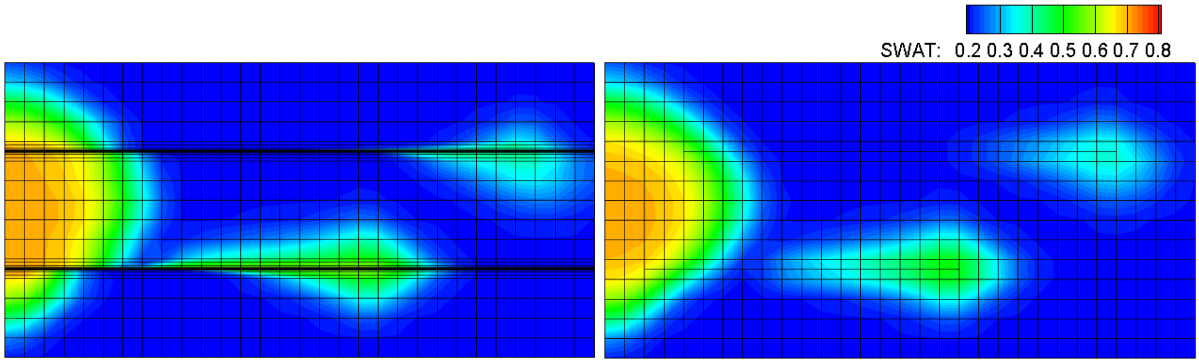

Figure 4.8. Water saturation distribution comparison: (a) Reference solution and (b) EDFM

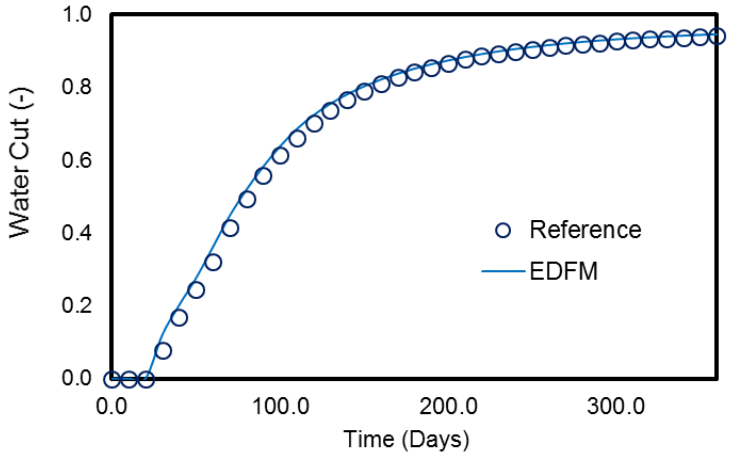

Figure 4.9. Water cut comparison

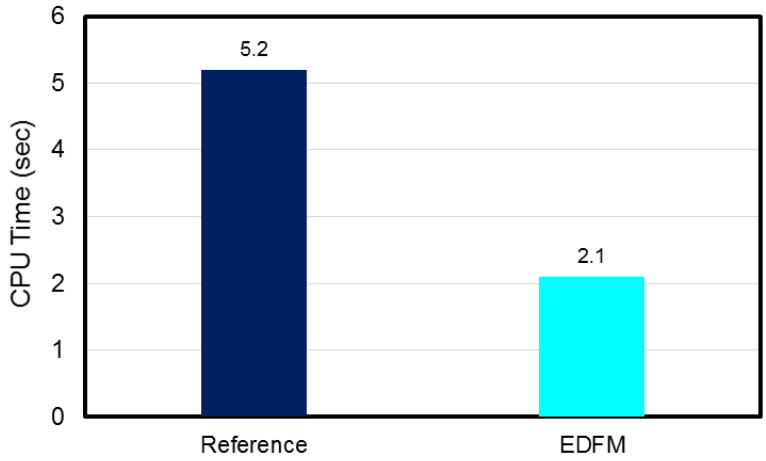

Figure 4.10. CPU Time comparison

Case 2: Water floods in a 2D reservoir with aligned intersecting fractures

This exercise is to validate implementation of NNCs for intersecting fractures. We used the same settings for the matrix domain as the previous example, whereas we have an additional intersecting fracture as illustrated in **Figure 4.11**. **Table 4.2** provides a summary of the reservoir properties. **Figure 4.12** and **Figure 4.13** compare pressure distributions and water saturation distributions between the reference solution and the EDFM solution. Water cut comparison is presented in **Figure 4.14**. Again the EDFM solutions show good agreement with the reference solutions. CPU time comparison is shown in **Figure 4.15** which indicates that the EDFM is faster than the fine scale reference solution, and is more significant compared with the previous example. It implies that the more geometry becomes complex (i.e., more fractures), the more benefits in the EDFM in terms of computational efficiency become significant.

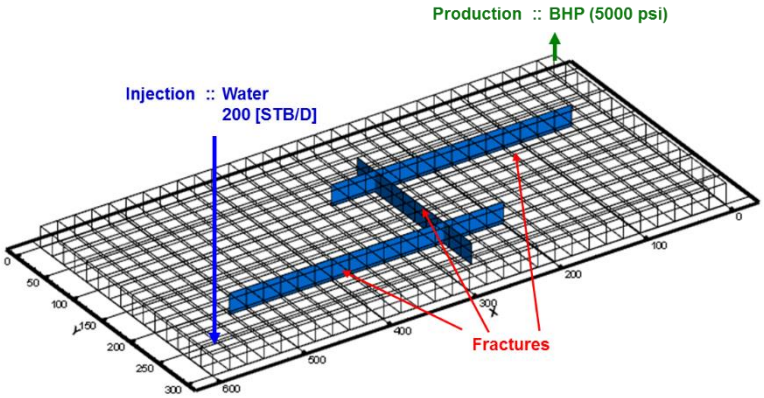

Figure 4.11. Schematic of the 2D aligned intersecting fractures

Table 4.2: Reservoir Properties of the Case 2

Parameter	Values
Matrix	
Permeability, mD	20.0
Porosity	0.10
Fracture	
Permeability, mD	7.00e+05
Porosity	0.010
Aperture, ft	0.0264

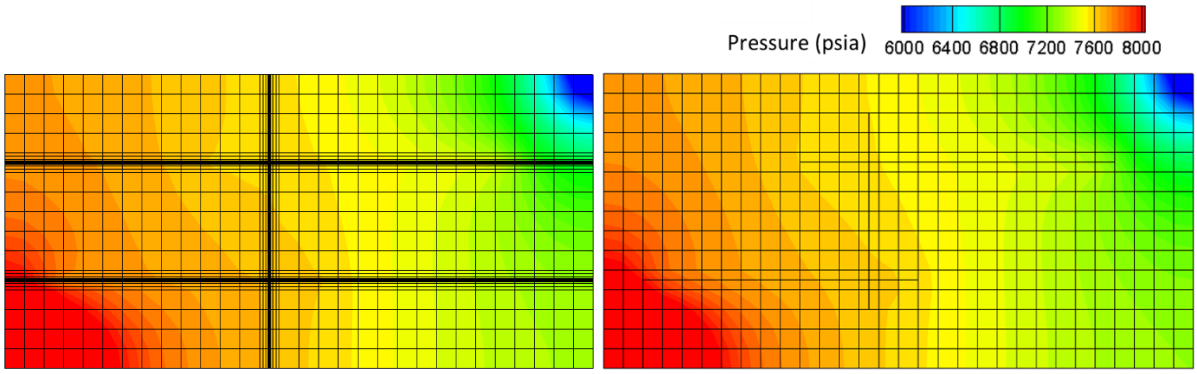

Figure 4.12. Pressure distribution comparison: (a) Reference solution and (b) EDFM

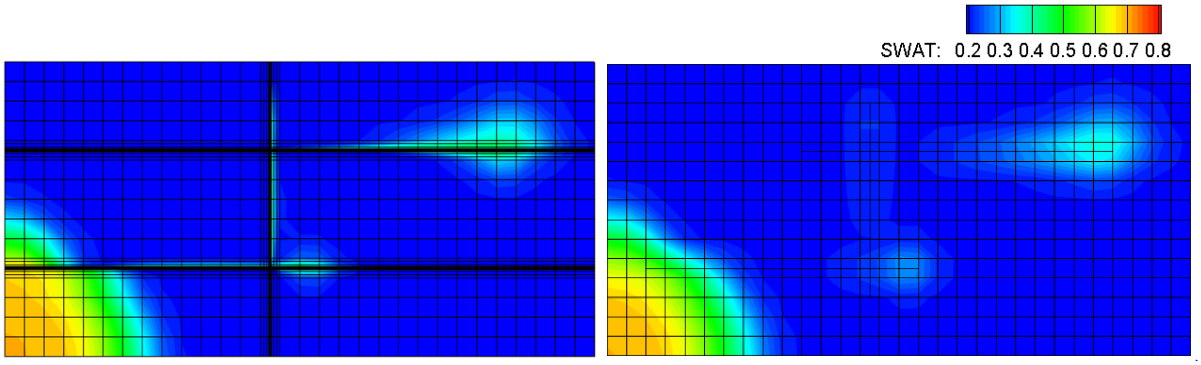

Figure 4.13. Water saturation distribution comparison: (a) Reference solution and (b) EDFM

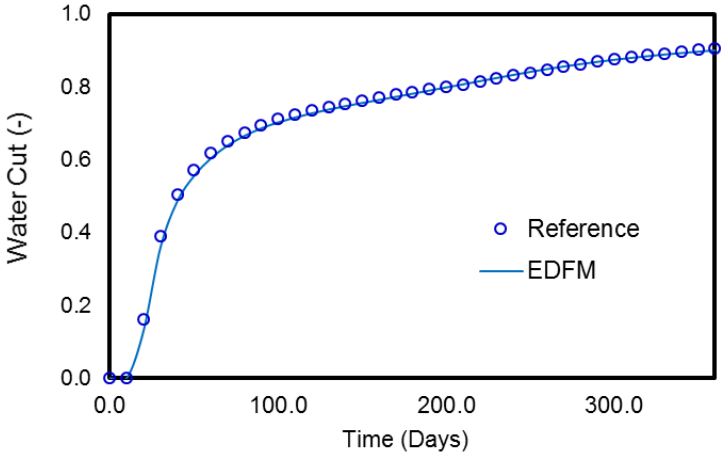

Figure 4.14. Water cut comparison

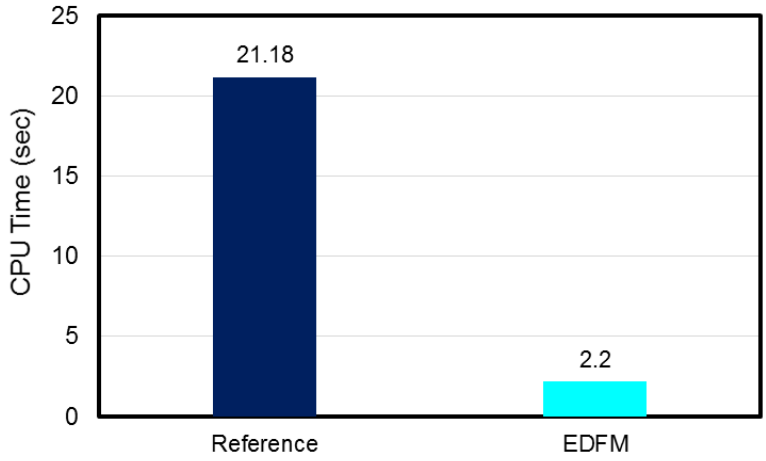

Figure 4.15. CPU Time comparison

Case 3: Water floods in a 2D reservoir with a 45 degree fracture

This example includes a non-aligned fracture to validate the accuracy of the EDFM for arbitrary-oriented fractures (Moinfar, et al. 2014). The reference solution in this example uses fine grids to describe a 45 degree fracture with permeability of 100.0 md as presented in **Figure 4.16**. The model discretized into 160 × 160 × 1, with average cell sizes of 0.025 × 0.025 × 0.025. For the EDFM, we prepared three cases with difference matrix gridblock discretization schemes including 80 × 80 × 1, 40 × 40 × 1, and 20 × 20 × 1 and placed an equivalent fracture to investigate matrix grid resolution sensitivity. In EDFM cases, size of matrix gridblocks are adjusted in accordance with the discretization scheme in such a way that the size of reservoir is consistent. Permeability at fracture gridblocks in the EDFM is adjusted to 70.7 md ($100.0/\sqrt{2.0}$) for fair comparisons. The same fluid model and relative permeability curves from the previous example are used. The model consists of a single injector and a single producer at corners (quarter 5 spot). The injector injects water with a constant rate (0.001

stb/day) constraint and boundary condition of the producer is 3000.0 psi BHP. In addition, brief descriptions of other reservoir properties are listed up in **Table 4.3**.

Table 4.3: Reservoir Properties of the Case 3

Parameter	Values
Matrix	
Permeability mD	1.0
Porosity	0.20
Fracture	
Permeability mD	1.00e+02
Porosity	0.020
Aperture, ft	0.050

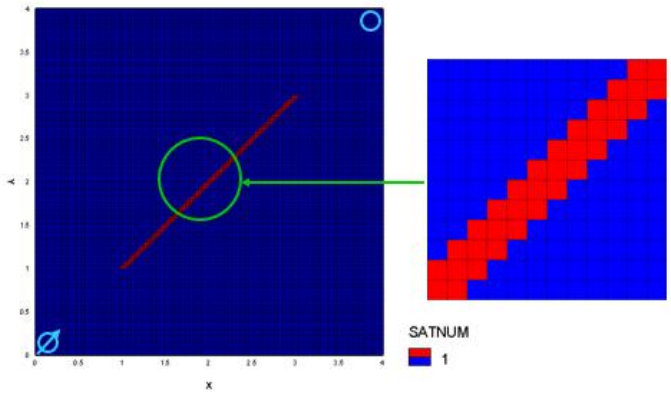

Figure 4.16: An illustration of the fine scale (160×160) reference solution

Figure 4.18 and **Figure 4.18** present comparisons of pressure distributions and water saturation distributions. The 80 × 80× 1 EDFM solution shows good agreement with the reference solution, whereas the EDFM solutions gradually start deviating from the reference solution as matrix grids become coarsened which can also be confirmed from the water cut comparison as shown in **Figure 4.19**. Errors in coarsened models may be simply because of

numerical dispersion and/or an assumption in the EDFM that matrix-fracture interactions are described by a local flow assumptions with a single transmissibility. In addition, CPU time is investigated as presented in **Figure 4.20**. While the reference solution takes approximately 100.0 seconds, the EDFM approaches only require less than 10 seconds. Through this exercise, it is found that the EDFM can reproduce the results of the fine scale reference solution without losing accuracy with moderate matrix grid coarsening. Computational efficiency of the EDFM is also confirmed.

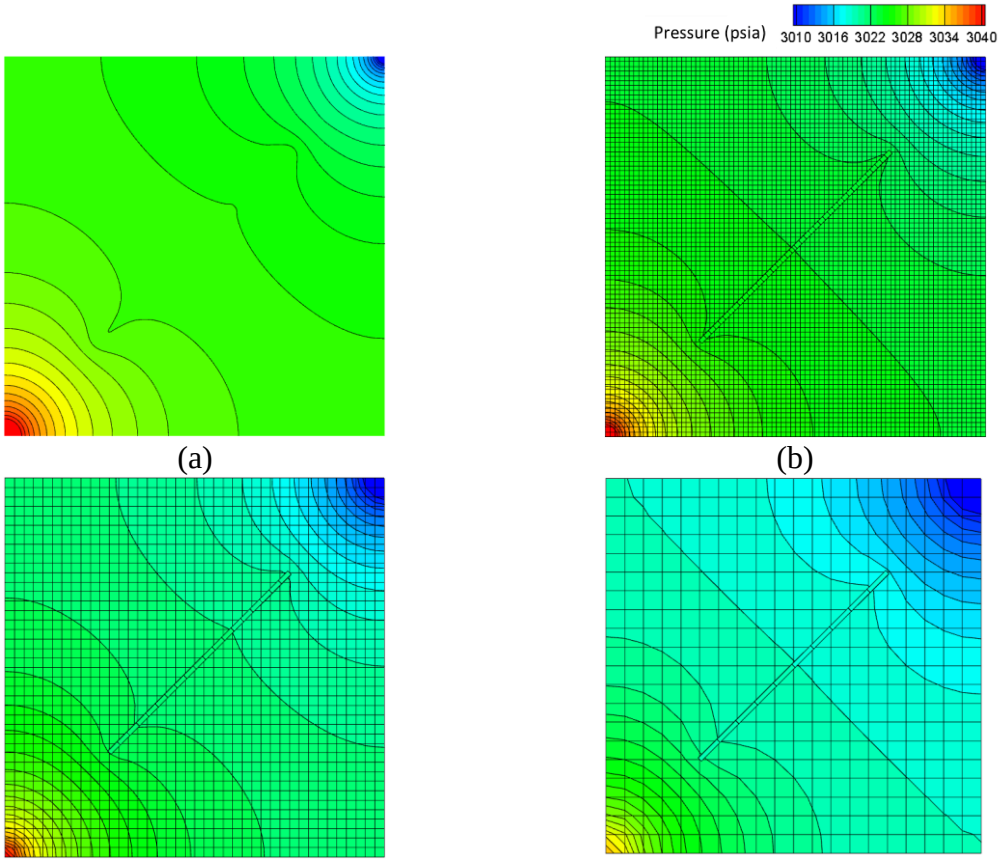

Figure 4.17: Comparison of pressure saturation distribution (a) the reference solution, (b) EDFM (80 × 80 × 1), EDFM (40 × 40 × 1), and EDFM (20 × 20 × 1)

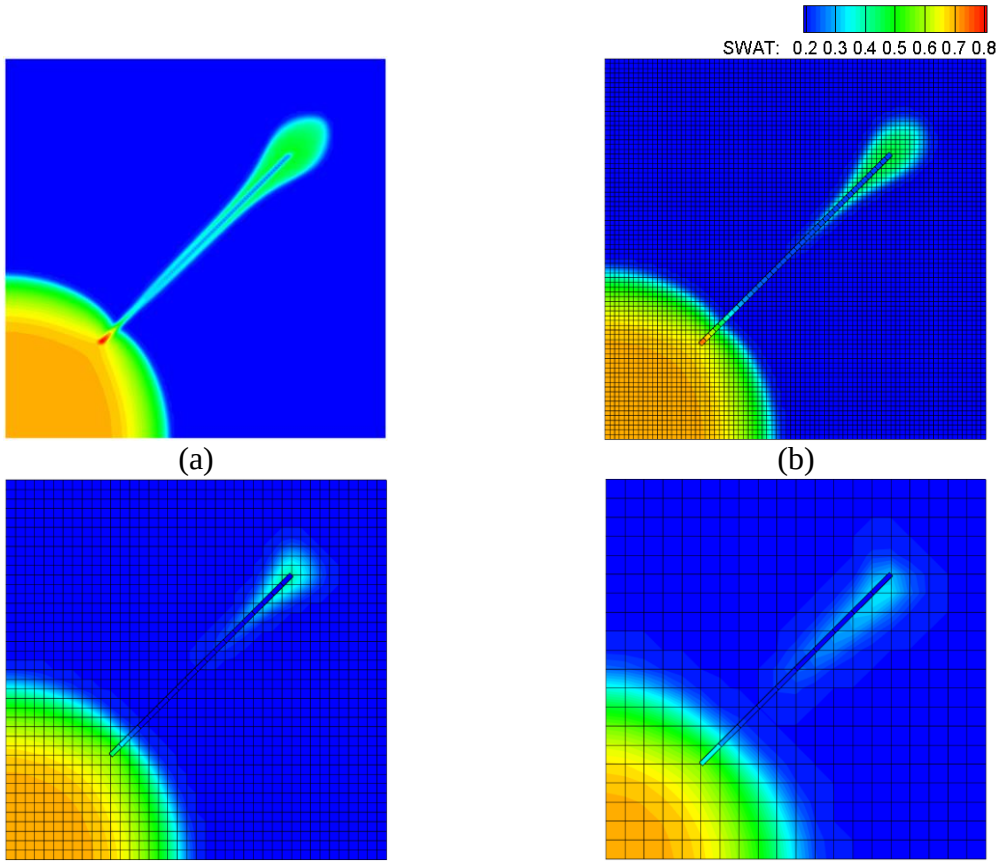

Figure 4.18: Comparison of water saturation distribution (a) the reference solution, (b) EDFM (80 × 80 × 1), EDFM (40 × 40 × 1), and EDFM (20 × 20 × 1)

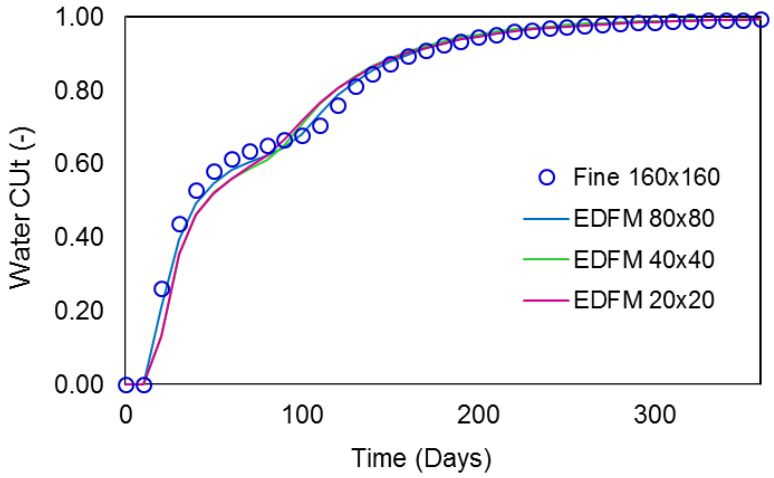

Figure 4.19: Comparison of water cut from the reference solution and EDFM solutions

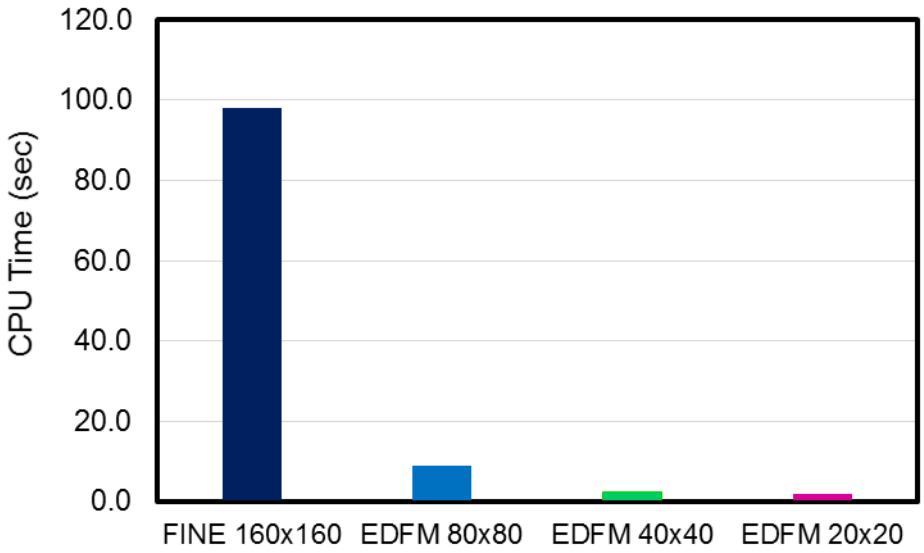

Figure 4.20: Comparison of CPU time

Case 4: 3D Horizontal Well with Multistage Fractures

We investigate the applicability of the EDFM in an unconventional reservoir development in this example. Brief reservoir properties are provided in **Table 4.3**. For the EDFM, the reservoir is discretized into 197 × 52× 5 with average cell sizes of 10.0 × 10.0 × 5.0 as illustrated in **Figure 4.21**. We have 15 hydraulic fractures and spacing is assumed to be uniform and the same half length (=150.0 ft). For the reference solution, we used fine-scale explicit fractures (tartan grid) to describe equivalent fractures. The fluids are assumed to be single phase gaseous and an isothermal system. The model consists of a single producer with 3000.0 psi BHP constraint. The results are presented in **Figure 4.22** and **Figure 4.23**. The EDFM solutions show great agreement with the reference solution in terms of pressure distributions and gas production rates. We confirmed the applicability of the EDFM in an unconventional reservoir development.

Table 4.4: Reservoir Properties of the Case 4

Parameter	Values
Matrix	
Permeability, mD	5.00e-04
Porosity	0460
Fracture	
Permeability, mD	1.00e+03
Porosity	0.0460
Aperture, ft	0.050
Spacing, ft	100.0

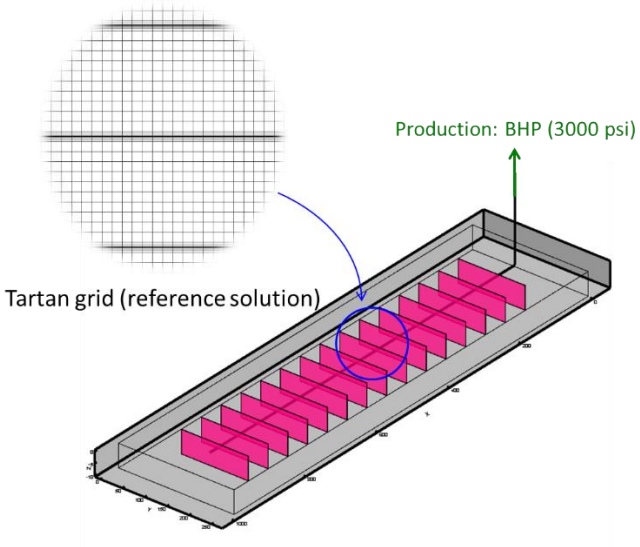

Figure 4.21: Schematic of 3D horizontal well case

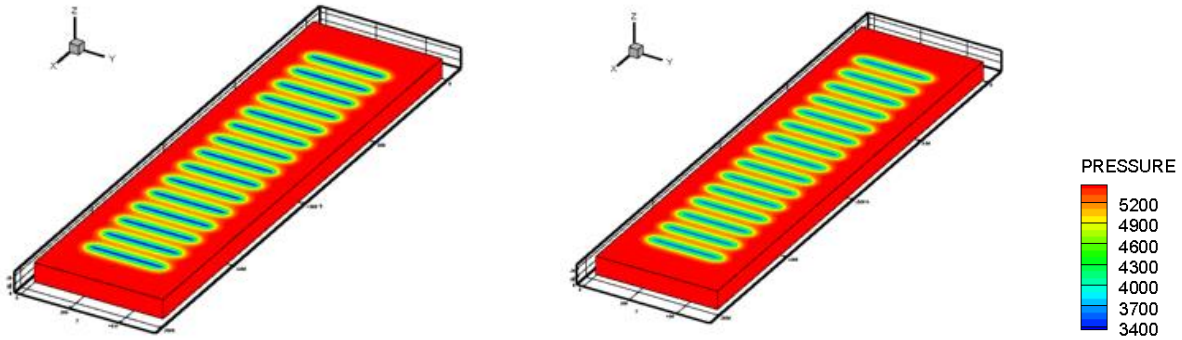

(a) Reference (b) EDFM

Figure 4.22: Pressure distribution comparison at 1 year

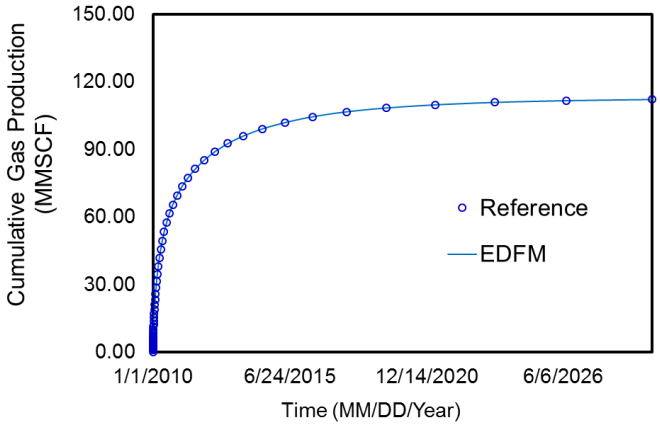

Figure 4.23: Cumulative gas production comparison

Case 5: Huff-and-Puff in 3D Horizontal Well with Multistage Fractures

We discuss here CO_2 huff-and-puff in a multistage hydraulically fractured well to demonstrate the applicability of the EDFM with compositional models (Iino, et al. 2017). Same settings from the case 3 is used for geometry but permeability and porosity are heterogeneous in this exercise (

Figure 4.24). The fracture porosity and permeability are assumed to be homogeneous and provided in **Table 4.4**. The fluids are assumed to be a three-phase compositional model including 7 components and assumed to be an isotherm system. **Table 4.5** presents details about the fluid model based on (Wan and Sheng 2015, Iino, et al. 2017). In addition, the three phase relative permeabilities based on (Siripatrachai, Ertekin and Johnes 2017) are illustrated in **Figure 4.25**. Capillary pressure is assumed to be negligible for simplicity. The initial pressure and reservoir temperature are set to be 4,500.0 psi and 160.0 Deg F, respectively. The bubble point of the fluid is 2,300.0 psi at the reservoir temperature. Prior to commencing the Huff-and-Puff operation, we performed slim tube tests which indicate that the minimum miscibility pressure (MMP) between and the reservoir fluid and pure CO_2 solvent is

approximately 2200.0 psi. The operation starts with a primary depletion with 2500.0 psi BHP constraint, followed by three cycles of (i) CO_2 injection (Huff) with 3500 psi BHP constraint for 25 days. (2) shut-in for 20 days, and (iii) production (Puff) with 2500.0 psi BHP constraint for 100 days. **Figure 4.27** compares pressure distributions between the reference solution and the EDFM solutions. In addition, **Figure 4.27** shows a comparison of oil production and CO_2 injection. The EDFM results show good agreement with the reference solutions. Through this exercise, we confirmed the applicability of the developed model to a compositional model in an unconventional reservoir.

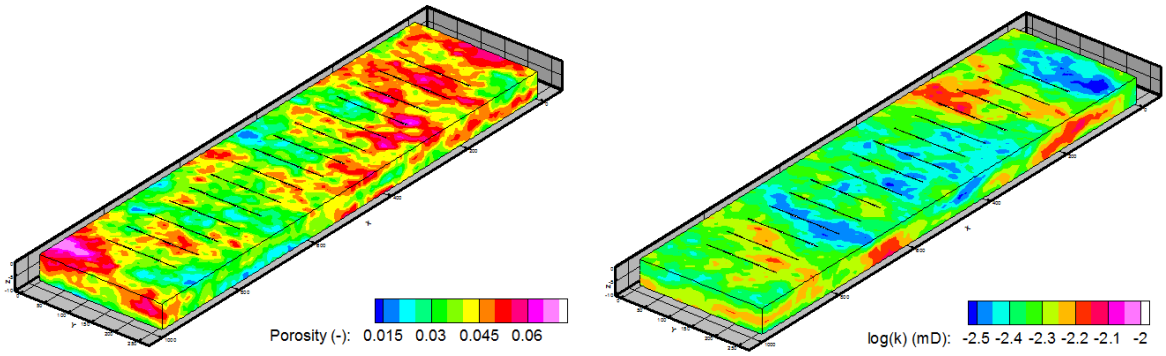

(a) (b)

Figure 4.24: Illustrations of (a) Porosity distribution, (b) Permeability distribution

Table 4.5: Reservoir Properties of the Case 5

Parameter	Values
Porosity	0.076
Permeability, mD	10.0
Aperture, ft	0.10
Half length, ft	75.0
Spacing, ft	55.0

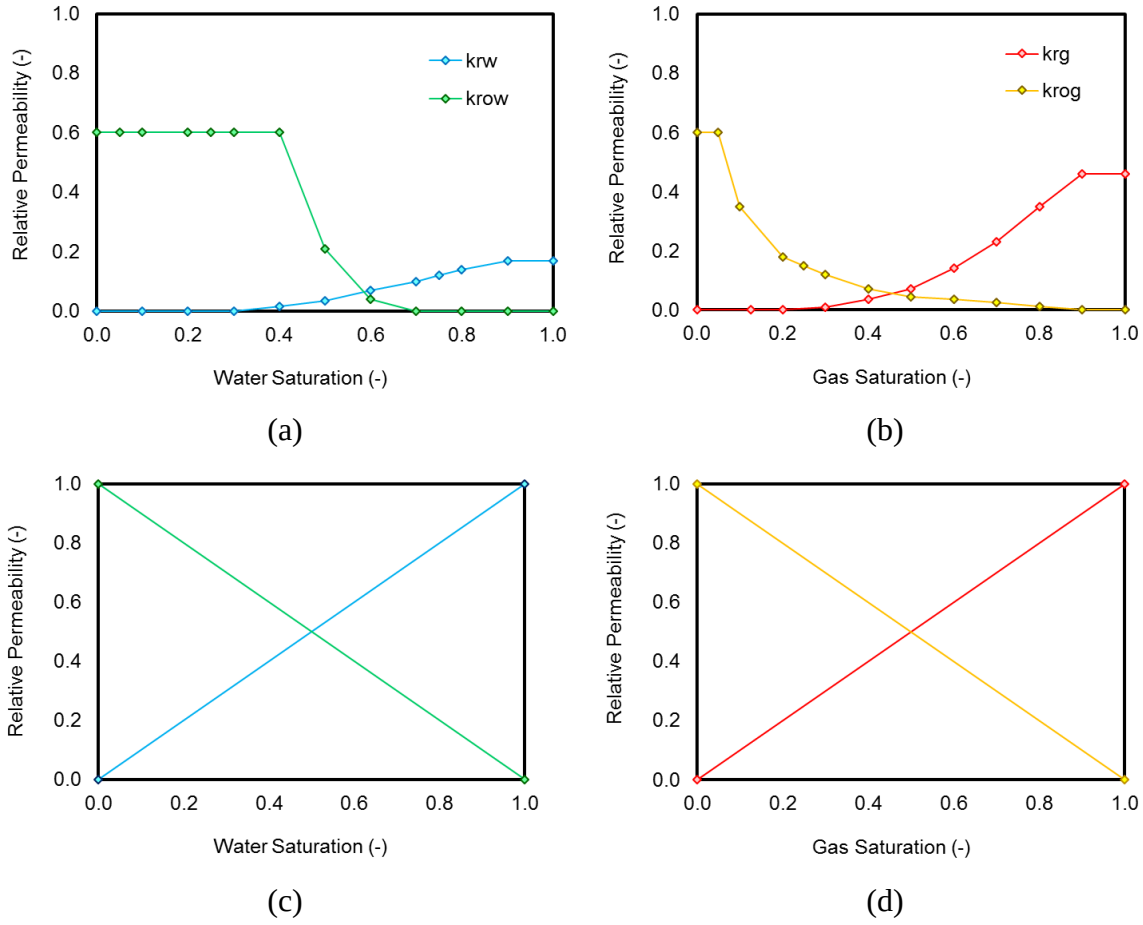

Figure 4.25: Three phase relative permeability curves, (a) water-oil in matrix, (b) gas-oil in matrix, (c) water oil in fracture, and (d) gas-oil in matrix

Table 4.6: Parameters in the fluid model

(a) Initial composition and EoS parameters

Component	Initial comp	Pc (psia)	Tc (R)	Acentric Factor	MW	Vc (ft^3/lb-model)
C1	0.50	667.79	343.08	0.013	16.00	0.0998
CO2	0.00	1069.87	547.56	0.225	44.01	0.0940
C2-3	0.03	616.35	665.64	0.152	44.10	0.2005
C4-6	0.07	436.91	913.32	0.300	86.20	0.3698
C7-11	0.20	304.06	1111.86	0.488	152.3	0.6297
C12-15	0.15	200.01	1270.08	0.650	203.0	1.0423
C16+	0.05	161.95	1380.06	0.850	282.0	1.3412

(b) Binary interaction coefficients

Component	C1	CO2	C2-3	C4-6	C7-11	C12-15	C16+
C1	-	0.103	0.0	0.0	0.0	0.05	0.05
CO2	0.103	-	0.135	0.0	0.0	0.0	0.0
C2-3	0.0	0.135	-	0.0	0.0	0.005	0.005
C4-6	0.0	0.0	0.0	-	0.0	0.0	0.0
C7-11	0.0	0.0	0.0	0.0	-	0.0	0.0
C12-15	0.05	0.0	0.005	0.0	0.0	-	0.0
C16+	0.05	0.0	0.005	0.0	0.0	0.0	-

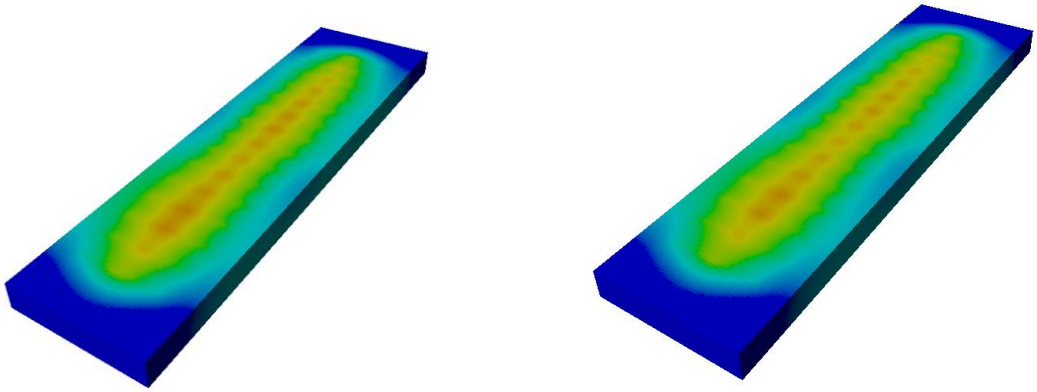

(a) (b)

Figure 4.26: Pressure distribution comparison: (a) The reference solution and (b) the EDFM solution at the end of the first cycle

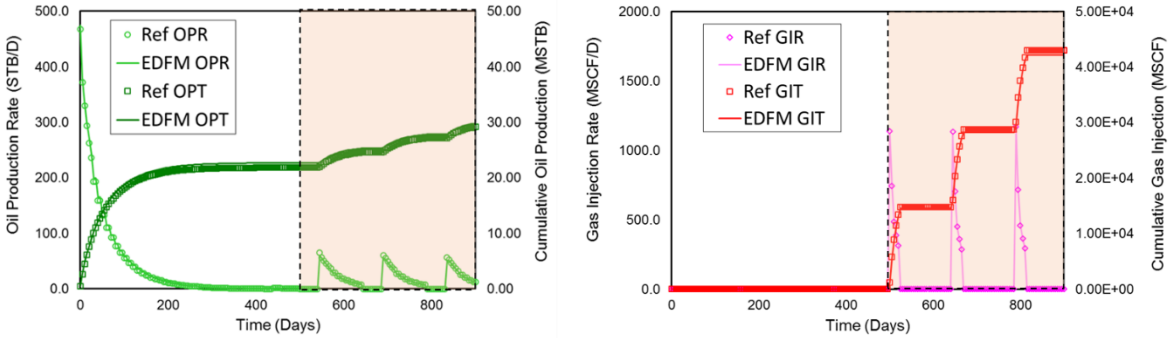

(a) (b)

Figure 4.27: EDFM solutions compared with the reference solutions (a) oil productions and (b) CO_2 injections

CHAPTER V

SUMMARY AND PATH FORWARD

5.1 Summary

In Chapter I-III, we have presented the calibration of a high resolution CO_2 EOR reservoir model. Our reservoir model calibration workflow relies on a novel reparameterization technique. Reservoir pressure and injection/production volumes were integrated into the model to understand the reservoir energy and drive mechanisms in the reservoir. For this purpose, we divided the reservoir into geologic regions using a spectral clustering technique that naturally defines the region boundaries based on the underlying heterogeneity patterns. Calibrated reservoir parameters obtained from this step shows consistency with geologic knowledge and laboratory data. Higher energy support from the bottom aquifer drive compared to the edge aquifer was confirmed based on the results obtained. These findings are consistent with opinions of the operator. We recently received downhole pressure monitoring data obtained from recent reservoir pressurizations from the operator. Although not shown here, we have calibrated the measurements using another parameterization technique, Grid Connectivity Transform (GCT) which permits a low rank representation of a model property distribution (Olalotiti-Lawal, Onishi, et al. 2017). There are several lessons learnt from the model calibration:

- We confirmed that the applicability of upscaling and validation workflow using our in-house software (SWIFT) (S. Du 2012) and DESTINY in a high resolution field application.

- We confirmed the applicability of our model calibration workflow, a hierarchical approach using a novel parameterization technique in a field application involving challenges including high heterogeneity and high uncertainties.
- In the sensitivity study, we found that pore volume multipliers, especially at region 2 which contains the largest amount of hydrocarbon are important. This may be because pore volumes can significantly contribute to reservoir energy and it is consistent with the objective function. Relative permeability parameters including the exponent for oil relative permeability curve and the end-point for the water relative permeability are also important parameters. It implies that multiphase flow plays an important role in the scenario and it is also consistent with the objective function consisting of misfits of pressure, oil production, and liquid production.
- Reservoir energy match resulted in local well-by-well match. It suggests that the reservoir is highly connected. However, matches at some wells show discrepancies. We recently received fresh water injection and CO_2 injection data from the operator and are currently working on history matching of these data. We may be able to improve local matches after this calibration.

In Chapter IV, we presented the implementation and validations of the EDFM approach. The implementation has been validated by comparing the EDFM approach with fine scale explicit fractures in both NFRs and unconventional reservoirs. We applied the developed model to a CO_2 Huff-and-Puff in a hydraulic fractured well case which showed the applicability of the developed model for multi-phase compositional model. Findings are following:

- Examples in NFRs and unconventional reservoirs with different scenarios (water injection, primary depletion, and Huff-and-Puff) demonstrated the applicability and robustness of our developed model.
- The EDFM approach is faster than the fine scale explicit fracture cases. The more complex fracture distribution we have, the more the computational efficiency in the EDFM becomes appreciable.
- The EDFM works well as long as matrix grid coarsening scheme is moderate. We confirmed that the aggressive matrix coarsening can lose accuracy.

5.2 Path Forward

The CO_2 EOR Project

We have calibrated reservoir pressure/energy over the period of prolonged depletion of the reservoir and then updated the model permeability field by utilizing the more recent water injection and pressure data for repressurization (not shown here). The operator recently conducted CO_2 floods in the pilot area and measured liquids and gas production data and tubing head pressure data. Our next step is to calibrate these recently measured data and then perform optimizations. Because reservoir pressure and energy have been matched, the streamline-based history matching may be a suitable approach to perform local updates (He, Yoon and Datta-Gupta 2002, Tanaka, Kam and Datta-Gupta, et al. 2015). After the local updates, we will work on optimizations of CO_2 floods in the pilot area. Our current plan is to apply the Design of Experiments (DoE)-based approach (Bhark and Dehgnani 2014) to investigate parameters which can impact on CO_2 floods such as the amount of CO_2 injected, the number of water

alternating gas (WAG) ratios, voidage replacement ratio (VRR), and WAG ratios (Bermudez, Johns and Parakh 2007). The operator plans to expand CO_2 flood patterns based on the pilot area and therefore our goal is to optimize the field scale CO_2 EOR operations.

The Embedded Discrete Fracture Model

We have demonstrated the implementation and validations of the EDFM. Our next steps include applications of the developed model. There are several ongoing ideas.

Streamline tracing on the EDFM

Streamline-based methods are useful tool for a variety of applications including modeling, inversion, and optimizations (Thiele and Batycky 2003, Alhuhali, Oyerinde and Datta-Gupta 2008, Datta-Gupta and King 2007, Park and Datta-Gupta 2011, Tanaka, Kam and Datta-Gupta, et al. 2015, Tanaka, Kam and Wang, et al. 2017). However, these approaches require streamline tracing which can be problematic in irregular meshing/gridding such as degenerate or highly distorted hexahedral cells, faults, pinchouts, and local grid refinement (LGR) interfaces. In recent years, because of the advent of the hydraulic fracturing and the horizontal well to develop unconventional resources, more and more reservoir models tend to employ these irregular shape of gridblocks to accurately describe fluid flow in fractures. As mentioned in Chapter IV, the EDFM approach is a promising alternative of conventional fracture modeling approaches and therefore it is an active are of research. Some industries recently have applied the EDFM in field scale studies (Du, Liang and Lin 2017). More and more applications of the EDFM approach in field case studies can be expected. Several authors introduced streamline tracing algorithms in these irregular gridblocks (Martringe, Juanes and Tchelepi 2008, Zhang, King and Datta-Gupta 2011), however, streamline tracing algorithm on

the EDFM has not been developed yet. Our next step is therefore to develop the streamline tracing algorithm on the EDFM which is beneficial because we can take full advantage of streamline-based technologies we have in our research group including forward modeling, history matching, and optimizations on the EDFM.

Fracture Characterization using the EDFM

Fracture distributions and properties usually entail high uncertainities although there are several techniques to detect fracture distributions available (e.g., micro seismic). Therefore, stochastic approaches may be suitable to characterize fractures. Computational efficiency and simple meshing as discussed in Chapter IV in the EDFM are preferable for stochastic frameworks requiring large number of realizations for numerical simulations.

REFERENCES

Alhuhali, A. H., D. Oyerinde, and A. Datta-Gupta. 2008. "Optimal Waterflood Management Under Geologic Uncertainty." *SPE Improved Oil Recovery.*

Allan, Jack, and S.Qing Sun. 2003. "Controls on Recovery Factor in Fractured Reservoirs: Lessons Learned from 100 Fractured Fields." *Annual Technical Conference and Exhibition.*

Bermudez, Leonardo, Russel T. Johns, and Harshad Parakh. 2007. "Parametric Investigation of WAG Floods Above the MME." *SPE Journal* 224-234.

Bhark, Eric W., A. Rey, A. Datta-Gupta, and B. Jafarpour. 2011. "Multiscale Parameterization and History Matching in Structured and Unstructured Grid Geometries." *SPE Reservoir Simulation Symposium.*

Bhark, Eric W., Behnam Jafarpour, and Akhil Datta-Gupta. 2011. "A Generalized Grid Connectivity-based Parameterization for Subsurface Flow Model Calibration." *Water Resources Research.*

Bhark, Eric, Akhil Datta-Gupta, and Behnam Jarapour. 2011. *SPE Annual Technical Conference and Exhibition.*

Bhark, Eric, and Kaveh Dehgnani. 2014. "Assited History Matching Benchmarking: Design of Experiments-based Techniques." *SPE Annual Technical Conference and Exhibition.*

Blaskovich, F. T., G. M. Cain, Fernand Sonier, David Waldren, and S. J. Webb. 1983. "A Multicomponent Isothermal System for Efficient Reservoir Simulation." *SPE.*

Brooks, R. H., and A. T. Corey. 1964. "Hydraulic Properties of Porous Media." *Hydrology Papers Colorado State University.*

Calsep. n.d. *PVTSim Nova.* https://www.pvtsimnova.com/.

Chai, Z., B. Yan, J. E. Killough, and Y. Wang. 2016. "An Efficient Method for Fractured Shale Reservoir History Matching: The Embedded DIscrete Fracture Multi-Continuum Approach." *SPE Annual Technical Conference and Exhibition.*

Datta-Gupta, A., and M. J. King. 2007. "Streamline Simulation: Theory and Practice." *SPE.*

Dean, R. H., and L. L. Lo. 1988. "Simulations of Naturally Fractured Reserovoirs." *SPE* 638-648.

Du, S, B Liang, and Y Lin. 2017. "Field Study: Embedded Discrete Fracture Modeling with Artificail Inteligence in Permian Basis for Shale Formation." *SPE Annual Technical Conference and Exhibition.*

Du, S. 2012. "Multiscale Reservoir Simulation: Layer Design, Full Field Pseudoization and Near Well Modeling." *Dissertation.*

Durlofsky, L.J., R.A. Behrens, R.C. Jones, and A. Bernath. 1996. "Scale Up of Heterogeneous Three Dimensional Reservoir Descriptions." *SPE Journal* 313.

Filho, Cavalcante, M. Moinfar J. S. A. Shakiba, and Kamy Sephehrnoori. 2015. "Implementation of a Preprocessor for Embedded Discrete Fracture Modeling in an IMPEC COmpositional Reservoir Simulator." *SPE Reservoir Simulation Symposium.*

GCCS. 2015. "The Global Status of CCS Summary Report 2015."

Hajibeygi, Hadi, Dimitris Karvounis, and Patrick Jenny. 2011. "A Hierarchical Fracture Model for the Iterative Multiscale Finite Volume Method." *Journal of Computational Physics* 8729-8743.

He, Zhong, Seongsik Yoon, and Akhil Datta-Gupta. 2002. "Streamline-based Production Data Integration WIth Gravity and Changing Field Conditions." *SPE Journal* 423-436.

Hill, A. C., and G. W. Thomas. 1985. "A new Approach for Smulationg Complex Fractured Reservoirs." *SPE.*

Hill, M. C. 2000. "Methods and Gudelines for Effective Model Calibration." *In Building Partnerships, edition* 1-10.

Hui, M, B Mallison, M Heidary-Fyrozjaee, and W Narr. 2013. "The upscaling of discrete fracture models for faster, coarse-scale simulations of IOR and EOR processes for reservoirs." *SPE Annual Technical Conference and Exhibition.*

Hui, Mun-Hong Robin, Mohammad Karimi-Fard, Bradley Mallison, and Louis J. Durlofsky. 2017. "A General Modeling Framework for Simulating COmplex Recovery Processes in Fractured Reservoirs at Different Resolutions." *SPE Reservoir Simulation Conference.*

Hyman, Jeffrey D., Satish Karra, Natallia Makedonska, Carl W. Gable, Scott L. Painter, and Hari S. Viswanathan. 2016. "DFNWORKS: A Discrete fracture network for modeling subsurface flow and transport." *Computers & Geosciences* 10-19.

Iino, Atsushi, Aditya Vyas, Jixiang Huang, Akhil Datta-Gupta, Yusuke Fujita, and Sathish Sankaran. 2017. "Rapid Compositional Simulation and History Matching of Shale Oil Reservoirs Using the Fast Marching Method." *URTec.*

Jafarpour, B., and D.B. McLauglin. 2009. "Reservoir Characterization With the Discrete Cosine Transform." *SPE Journal* 182-201.

Jiang, Jiamin, and Rami M. Younis. 2016. "Hybrid Coupled DIscrete-Fracture/Matrix and Multicontinuum Models for Unconventional Reservoir Simulation." *SPE Journal* 1009-1027.

Kang, SukSang, Eric Bhark, Akhil Datta-Gupta, JangHak Kim, and LiSik Jang. 2014. "A Hierarchical Model Calibration Approach with Multiscale Spectral-Domain Parameterization: Application to a Structurally Complex Fractured Reservoir." *SPE Improved Oil Recovery SYmposium.*

Karimi-Fard, M., L. J. Durlofsky, and K. Aziz. 2004. "An Efficient Discrete-Fracture Model Applicable for General-Purpose Reservoir Simulators." *SPE Journal* 227-236.

Karimi-Fard, M., L.J. Durlofsky, and K. Aziz. 2004. *SPEJ* 227-236.

Kazemi, H., Jr L.S. Merrill, and P.R. Zeman. 1976. "Numerical Simulation of Water-Oil Flow in Naturally Fractured Reservoir." *SPEJ* 317.

King, M. J., K. S. Burn, Pengju Wang, V. Muralidharan, F. Alvarado, X. Ma, and Akhil. Datta-Gupta. 2005. "Optimal Layer Coarsening of 3D Reservoir Models for Flow Simulation." *SPE Annual Technical Conference and Exhibition.*

Leverett, M. C. 1941. "Capillary Pressure in Porous Solids." *Transactions of the AIME* 152-169.

Li, D., and B. Becker. 2000. "Optimal Uplayering for Scaleup of Multimillion-Cell Geologic Models." *SPE Annual Technical Conference and Exhibition.*

Li, L, and S. H Lee. 2008. "Efficient field-scale simulation for black oil in a naturally fractured reservoir via discrete fracture networks and homogenized media." *SPE Reservoir Evaluation & Engineering* 750-758.

Loeve, M. 1977. *Probability Theory I.* Springer.

Ma, Xianlin, Mishal Al-Harbi, Akhil Datta-Gupta, and Yalchin Efendlev. 2008. "An Efficient Two-Stage Sampling Method for Uncertainty Quantification in History Matching Geological Models." *SPE Journal* 77-87.

Ma, Xianlin. 2008. "History Matching and Uncertainty Quantification Using Sampling Method." *Dissertation.*

Madiebo, Kingsley I., Hadi Nasrabadi, and Eduardo Gildin. 2015. "Mesoscopic Simulation of Slip Motion for Gas Flow in Nanochannels." *ASME 2015 International Mechanical Engineering Congress and Exposition.*

Martringe, S., R. Juanes, and H. A. Tchelepi. 2008. "Tracing Streamlines on Unstructured Grids From Finite Volume Discretizations." *SPE Journal* 423-431.

Moinfar, A, A Varaveri, Sepehrnoori, and R. T Johns. 2014. "Development of an efficient embedded discrete fracture model for 3D compositional reservoir simulation in fractured reservoirs." *SPE Journal* 289-303.

Moinfar, Ali, Wayne Narr, Mun-Hong Hui, Bradley Mallison, and Seong H. Lee. 2011. "Comparison of Discrete-Fracture and Dual-Perneability Models for Multiphase Flow in Naturally Fractured Reservoirs." *SPE Simulation Symposium.*

Monteagudo, J. E. P., and A. Firoozabadi. 2004. "COntrol-volume method for numerical simulation of two-phase immiscible flow in two- and three-phase dimsneional discrete-fractured media." *Water Resources Research.*

Moridis, George J., and Craig M. Freeman. 2013. "The RealGas and RealGasH2O options of the TOUGH+ code for the simulation of coupled fluid and heat flow in tight/shale gas systems." *Computers & Geosciences* 56-71.

Noorishad, J, and M Mehran. 1982. "An Upstream finite element method for solution of transient transport equation in fractured porous media." *Water Resources Research* 588-596.

Olalotiti-Lawal, Feyi, and Akhil Datta-Gupta. 2015. *SPE Annual Technical Conference and Exhibition.*

Olalotiti-Lawal, Feyi, Tsubasa Onishi, Akhil Datta-Gupta, Yusuke Fujita, and Kenji Hagiwara. 2017. "Post-Combustion CO_2 COR Development in a Mature Oil Field: Model Calibartion Using a Hierarchical Approach." *SPE Annual Technical Conference and Exhibition.*

Panfili, P., and A. Cominelli. 2014. "Simulation of Miscible Gas Injection in a Fractured Carbonate Reservoir using an Embedded Discrete Fracture Model." *Abu Dhabi International Petroleum Exhibition and Conference.*

Park, H., and A. Datta-Gupta. 2011. "Reservoir Management Using Streamline-based Flood Efficiency Maps and Application to Rate Optimization." *SPE Western North American Regional Meeting.*

Park, Han-Young, Akhil Datta-Gupta, and Michael J. King. 2014. "Handing conflicting multiple objectives using Pareto-based evolutionary algorithm during history matching of reservoir performance." *Journal of Petroleum Science and Engineering* 48-66.

Pruess, and T. N, Narashiman. 1985. "A Practical Method for Modeling Fluid FLow in Fractured Media." *SPE Journal* 14-26.

Schlumberger. 2014. "ECLIPSE Reference Manual."

Shahvali, M., B. Mallison, K. Wei, and H. Gross. 2011. "An Alternative to Streamlines for Flow Disgnostics on Structures and Unstructures Grids." *SPE Annual Technical Conference and Exhibition.*

Siripatrachai, Nithiwat, Turgay Ertekin, and Russell T. Johnes. 2017. "Compositional Simulation of Hydraulically Fractured Tight Formation Considering the Effect of Capillary Pressure on Phase Behavior." *SPE Journal* 1046-1063.

Strang, Gilbert. 1999. "The Discrete Cosine Transform." *SIAM Review.*

Tanaka, S., Dongjae Kam, Akhil Datta-Gupta, and Michael J. King. 2015. "Streamline-based History Matching of Arrival Times and Bottomhole Pressure Data for Multicomponent Compositional Systems." *SPE Annual Technical Conference and Exhibition.*

Tanaka, S., Dongjae Kam, Zhiming Wang, Xian-Huan Wen, Kaveh Dehghani, Honquan Chen, and A. Datta-Gupta. 2017. "A Generalized Derivative-Free Rate Allocation Optimization for Water and Gas Flooding Using Streamline-Based Method." *SPE Annual Technical Conference and Exhibition.*

Tene, M., Sebastian B. B. Bosma, Mohammed Saad Al Kobaisi, and Hadi Hajibeygi. 2017. "Projection-based Embedded Discrete Fracture Model." *Advances in Water Resources* 205-216.

Thiele, Marco R., and Rod. O. Batycky. 2003. "Water Injection Optimization Using a Streamline-Based Workflow." *SPE Annual Technical Conference and Exhibition.*

Todd, M. R., and W. J. Longstaff. 1972. "The Development, Testing, and Application of a Numerical Simulator for Predicting Miscible Flood Performance." *Journal of Petroleum Technology* 874-882.

Wan, Tao, and James Sheng. 2015. "Compositional Modeling of the Diffusion Effect on EOR Process in Fractured Shale-Oil Reservoirs by Gas Flooding." *Journal of Canadian Petroleum Technology* 107-115.

Warren, J.E., and P.J. Root. 1963. "The Behavior of Naturally Fractured Reservoirs." *SPEJ* 245.

Whittaker, S., B. Rostron, C. Hawkes, C. Gardner, D. White, J. Johnson, R. Chalaturnyk, and D. Seeburger. 2011. "A decade of CO_2 injection into depleted oil fields: monitoring and research activities of the IEA GHG Weyburn-Midale CO_2 Monitoring and Storage Project." *Energy Procedia* 6069-6076.

Willhite, G. 1986. *Waterflooding, Volume 2 of spe Textbook series.* Richardson, TX: SPE.

Xu, Y., J. S. A. Cavalconate Filho, W. Yu, and K. Sepehrnoori. 2017. "Discrete-Fracture Modeling of COplex Hydraulic-Fracture Geometries in Reservoir Simulators." *SPE Reservoir Evaluation & Engineering* 403-422.

Yin, Jichao, Han-Young Park, Akhil Datta-Gupta, Michael J. King, and Manoj K. Choudhary. 2011. "A Hierarchical Streamline-assisted History Matching Approach with Global and Local Parameter Updates." *Journal of Petroleum Science and Engineering* 166-130.

Zhang, Y., M. J. King, and A/ Datta-Gupta. 2011. "Robust Streamline Tracing Using Intercell Fluxes in Locally Refined and Unstructured Grids." *SPE Reservoir Simulation Symposium.*

APPENDIX A

THE PREPROCESSOR

As discussed in the Chapter 4, we implemented the EDFM in ECLIPSE. In the EDFM approach, fractures are explicitly described in a separate computational domain as two-dimensional planes in addition to the matrix domain as illustrated in **Figure 4.1**. These fractures are discretized by the cell boundaries in the matrix domain. The fracture gridblocks are then linked with corresponding matrix gridblocks via non-neighbor connections (NNCs) which define additional connections between any gridblocks in finite-difference/volume framework. We applied NNC keyword in ECLIPSE to reproduce these procedures. The developed workflow is demonstrated with a simple example as follows:

1. Input

   In the step 1, we input geometry of matrix and fractures and necessary properties to compute transport index. For fractures, we input starting point, angle, length, and aperture. In our approach, input format is basically consistent with ECLIPSE. **Figure A-1** presents a sample input for matrix and fracture. Note that use can also input these through ECLIPSE NOSIM run (.INIT file and GRID/EGRID file). In **Figure A-1 (a)**, keywords are consistent with ECLIPSE. On the other hand, in the **Figure A-1 (b)**, it is necessary to specify several keywords to describe fractures:

   - `MAXNUMFRACELEM`: Maximum number of elements in the fracture domain. This keyword will be used to initialize necessary variables in the preprocessor.

- PERMXF: This keyword stands for fracture permeability. In this specific example, a single value is specified and is default setting. Then the preprocessor will assign uniform properties in fracture gridblocks. The reason why we use the default setting which only requires a single value is because the number of fracture elements is unknown without running the preprocessor which discretize fracture domain based on the matrix and fracture geometry. Note that there is a functionality to input cell-by-cell properties in the fracture domain which may be useful in situations where we want to investigate sensitivity of parameters in fracture domain (e.g., history matching, model ranking, etc.).
- POROF: This keyword stands for fracture porosity and has the same functionality as PERMXF.
- SWATF: This keyword stands for fracture initial water saturation. It also has the same functionality as PERMXF and POROF. We only have water saturation here in this specific example. However, it can also be extended for multiphase or multicomponent systems. Further, this keyword will be ignored if the initialization is set to be done by EQUIL keyword (Schlumberger 2014) in ECLIPSE runs.
- FRACSPEC: This keyword is to determine fracture geometry and consists of 7 parameters, I0, J0, K1, K2, angle, aperture, and length. The preprocessor will generate mesh and compute TI based on this input. Although not shown in this example, it can also be used for 3D cases in which we have additional parameters for K-direction. Note that our EDFM approach is currently limited to vertical fractures.

- DISCNUM: This keyword determines the discretization scheme for numerical integral calculations to compute < *d* >. The default value is 1000 which usually shows accurate results without losing computational efficiency.

```
RUNSPEC   ============================================================

TITLE
EDFM PREPROCESSOR
-- BY TSUBASA ONISHI 01/10/2017
-----------------------------------------------------------------------

DIMENS
5 5 1 /


GRID      ============================================================

DX
25*20.0
/

DY
25*20.0
/

DZ
25*10.0
/

TOPS
5000.0
/

PERMX
25*1.0
/

PORO
25*0.1
/

SOLUTION      ========================================================

PRESSURE
25*3000.0
/
SWAT
25*0.20
/
```

(a)

```
-------------------------------------------
EDFM
-------------------------------------------

MAXNUMFRACELEM
200
/

PERMXF
10000.0
/

POROF
0.01
/

SWATF
0.0001
/

-- I0 J0 K1 K2 ANGLE APERTURE LENGTH
FRACSPEC
20.0 50.0 1 1 0.0 0.0264 60
/

NUMDISC
100000
/
```

(b)

Figure A-1: Sample Input (a) Matrix and (b) fracture

2. The Preprocessor

The next step is to run the preprocessor. Results are illustrated in **Figure A-2** and **Figure A-3**. Details of the NNC keyword can be found in the ECLIPSE manual (Schlumberger, ECLIPSE Reference Manual 2014).

```
NNC
--------------------------
-- Matrix-Fractures
--------------------------
-- IM JM KM IF JF KF  TRAN
  2   3   1   1   7   1  0.09015098490151 /
  3   3   1   2   7   1  0.09015098490151 /
  4   3   1   3   7   1  0.09015098490151 /
-- End of fracture 1
  2   2   1   1   9   1  0.08687800101012 /
  2   3   1   2   9   1  0.01497105874395 /
  3   3   1   3   9   1  0.08676695785585 /
  3   4   1   4   9   1  0.01497105874395 /
-- End of fracture 2
--------------------------
-- Fracture-Fracture
--------------------------
-- IF1 JF1 KF1 IF2 JF2 KF2  TRAN
  2   7   1   3   9   1  2.18764843506747 /
-- End of intersecting fractures
 /
```

Figure A-2: NNC Keyword generated by the preprocessor

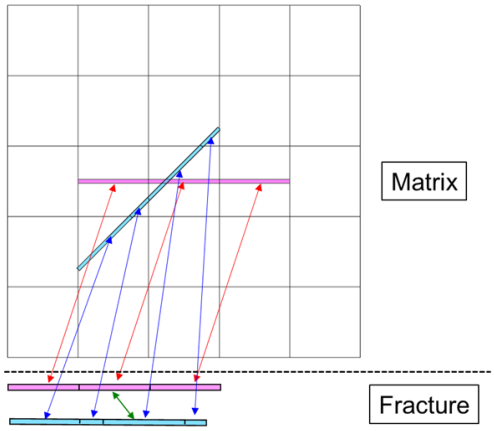

Figure A-3: Geometry

3. ECLIPSE

We provide updated geometry and the NNC keyword obtained from the step 2 for ECLIPSE runs. **Figure A-4** presents an illustration of the Jacobian in this example.

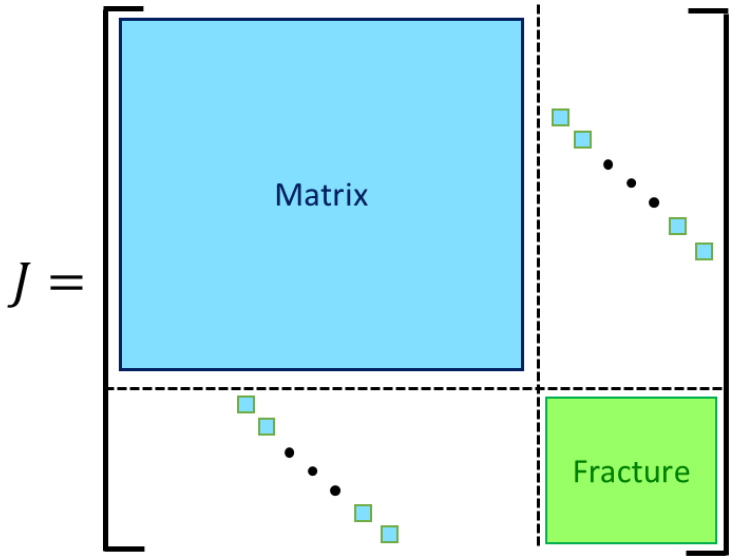

Figure A-4: Jacobian

APPENDIX B

AVERAGE NORMAL DISTANCE

One of key concepts in the EDFM approach is the average normal distance $< d >$ (Eq. 4.3) which will be used to compute transport index (TI) between a matrix and a fracture gridblocks. Prior to conduct validations of the implementation of the EDFM with fine scale explicit fracture cases (Chapter 4.3), we validated the implementation of $< d >$. Analytical solutions are available in simple geometries (Hajibeygi, Karvounis and Jenny 2011) which can be derived from simple integrations as illustrated in **Figure B.1** in which $< d >$ at bottom of each picture is an analytical expression for each geometry. **Table B-1** summarizes comparisons between analytical $< d >$ and computed $< d >$ using the preprocessor. Computed $< d >$ shows great agreement with analytical solutions.

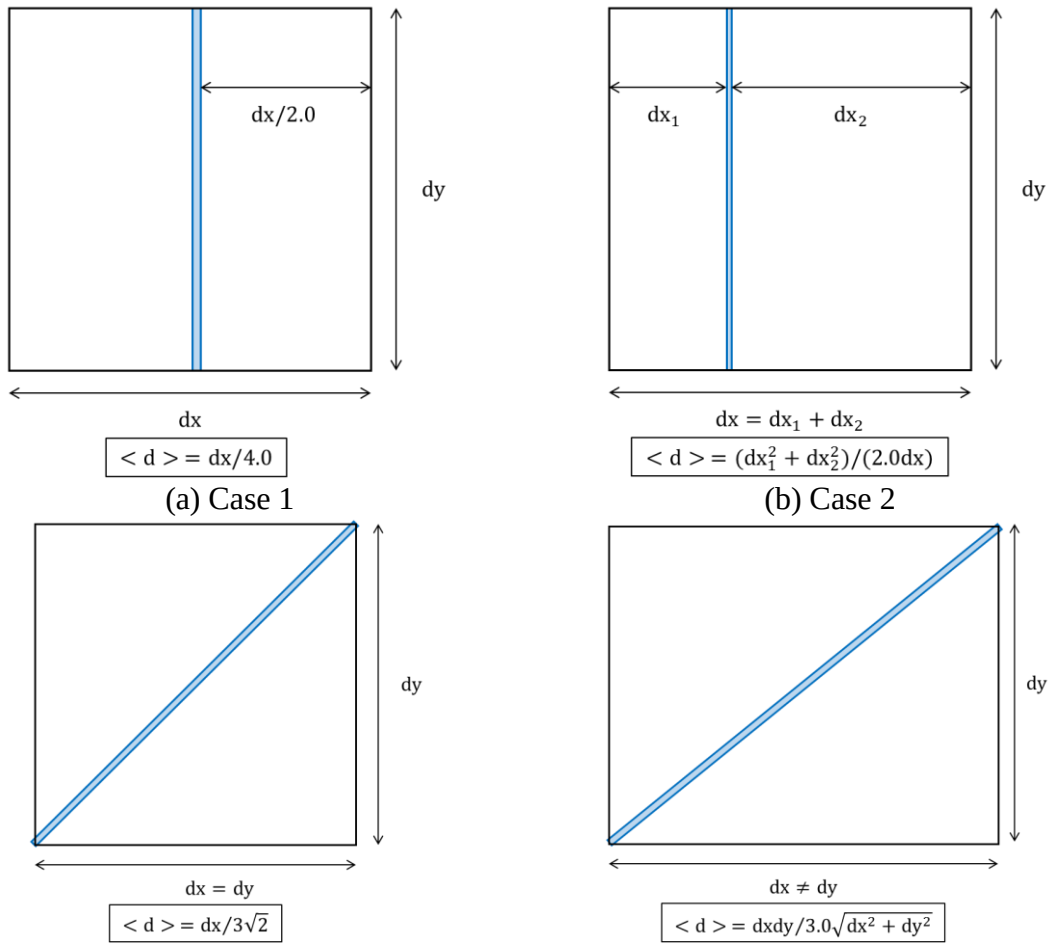

Figure B.1: (a) dx=dy, an aligned fracture, (b) $dx_1 \neq dx_2$, aligned fracture, (c) dx=dy, a diagonal fracture, and (d) dx≠dy, a diagonal fracture

Table B.1: Average normal distance comparison

	Case 1	Case 2	Case 3	Case 4
Analytical <*d*>	5.00	6.25	4.714045	2.88675
Computed <*d*>	5.00	6.25	4.713904	2.82600
Error	0.00	0.00	1.414e-4	6.075e-2

We further validated the implementation by comparing computed TI using the preprocessor with computed transmissibility obtained from ECLIPSE in which we applied Local Grid Refinement (LGR) to describe fractures. Although LGR is basically limited to aligned fractures, it is useful for validation purposes. In this exercise, we look at a single gridblock illustrated in **Figure B.2**. Results are summarized in **Table B.2**. Note that $2.0 \times T_{LGR}$ is physically equivalent to T_{EDFM} . The computed TI using the preprocessor shows great agreement with the transmissibility computed by ECLIPSE.

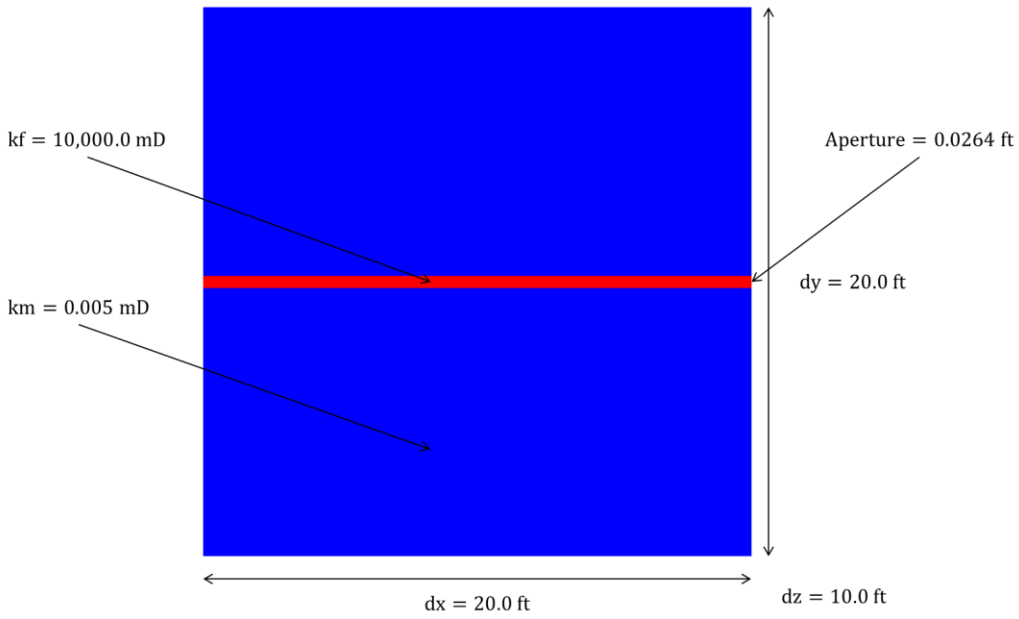

Figure B.2: An illustration of a single grid block containing a fracture

Table B.1: Average normal distance comparison

Parameter	Values
$2.0 \times T_{LGR}$	0.0004502
T_{EDFM}	0.0004508
Error	6.0000e-7